# Development of Iridium-Bismuth-Oxide Coatings for Use in Neural Stimulating Electrodes

by

Xingge Xu

Department of Chemical Engineering

McGill University, Montreal

April 2019

A thesis submitted to McGill University in partial fulfillment of the requirements of the degree of Master of Chemical Engineering

# Abstract

Implantable neural prosthetics with stimulating electrodes is an increasingly-employed medical practice to treat neural disability. Further development of prosthetics to recover complex neuron function requires electrodes with higher capacity to delivery charge to neuron. Ir-oxide is currently considered as state-of-the-art stimulating electrode material. However, further improvement of its properties is needed. Consequently, in this work, addition of bismuth to Ir-oxide to produce $Ir_xBi_{1-x}$-oxide coatings of various composition (x = 0, 0.2, 0.4, 0.6, 0.8 and 1.0) were fabricated by thermal deposition of their salts on a titanium substrate, and their charge-storage/delivery capacity, surface morphology, crystalline structure and biocompatibility was evaluated. The mixed metal oxides were characterized as consisting of multi-oxide states of Ir and Bi. It was found that only a 20mol.% addition of bismuth to Ir-oxide to produce $Ir_{0.8}Bi_{0.2}$-oixde yielded superior properties to Ir-oxide. This electrode exhibited a five-fold increase in charge storage capacity over the Ir-oxide electrode, yielding 26.8 $mC/cm^2$. At the same time, this electrode yielded the lowest impedance at 1 kHz. The superior performance of $Ir_{0.8}Bi_{0.2}$-oixde was explained to originate from change in lattice structure upon introduction of Bi to Ir-oxide, which enables better access of $H^+$ and $OH^-$ ions deeper into the oxide structure, thus yielding a higher charge storage capacity. The $Ir_{0.8}Bi_{0.2}$-oixde electrode also showed good stability and biocompatibility, which makes potentially a better candidate for neural stimulating electrodes than the current state-of-the-art Ir-oxide.

# Abrégé

Les prothèses neurales implantables avec électrodes de stimulation constituent une pratique médicale de plus en plus employée dans le traitement d'incapacité neurales. Le développement davantage de prothèses pour rétablir une fonction neuronale complexe nécessite des électrodes ayant une capacité plus élevée pour délivrer la charge au neurone. L'oxyde d'Ir est actuellement considéré comme un matériau d'électrode de stimulation supérieur. Cependant, une amélioration de ses propriétés est nécessaire. Pour cette raison, dans ce travail, l'addition de bismuth à l'oxyde de Ir pour produire des revêtements d'$Ir_xBi_{1-x}$-oxydes de compositions diverses (x = 0, 0,2, 0,4, 0,6, 0,8 et 1,0) ont été fabriquées par le processus bien établi « décomposition thermique » de leurs sels sur des titane substrats, et leur capacité de stockage/livre de charge, leur morphologie de surface, leur structure cristalline et leur biocompatibilité ont été évalués. Les oxydes métalliques mixtes fabriquées dans le projet ont constituées d'Ir et de Bi selon des technique de caractérisation. Il a été constaté que seule une addition de 20% en moles de bismuth à l'oxyde d'Ir pour produire de l'$Ir_{0.8}Bi_{0.2}$-oxyde donnait des propriétés supérieures à celles de l'oxyde d'Ir. Cette électrode présentait une capacité de stockage cinq fois plus élevé que l'électrode en oxyde d'Ir, ce qui donnait 26.8mC/cm$^2$. Au même temps, cette électrode produisait la plus faible impédance à 1 kHz. La performance supérieure d'$Ir_{0.8}Bi_{0.2}$-oixde est expliqué par le changement de structure du réseau lors de l'introduction de Bi dans l'oxyde d'Ir, ce qui permet un meilleur accès approfondi des ions H + et OH- à la structure de l'oxyde, produisant ainsi une capacité de stockage plus élevée. L'électrode Ir0.8Bi0.2-oxyde a également montré une bonne stabilité et une bonne biocompatibilité, ce qui fait en sorte que ce-dernier a la potentielle d'être un meilleur candidat pour les électrodes de stimulation neurale que l'oxyde d'Ir.

# Acknowledagements

First and foremost, I would like to thank my supervisor, Prof. Sasha Omanovic, for taking me as a master's student in his group and for the research opportunities that I have been given. Without his warm support, guidance and encouragement in both research and life, the work presented in this thesis would not have been possible.

Thanks to my colleagues Elmira and Mahmoud and technical staff Andrew and Ranjan for their instrumental help with characterization tests. Thanks to Dr Heather Durham and her group, especially to Sandra for performing the cytotoxicity test and for her patient instructing. Thanks to all members of the "Electrochemistry and Corrosion" lab for creating a fantastic environment that make this journey not that stressful and lonely, Special thanks to Elimra who introduced me to everything; to Mahmoud for his academic and linguistic help; and to Aqeel for his wise life suggestions. Thanks to Hao and Zhuoya who make these two years adventure more joyful and accompanied.

I would thank the McGill University and my department for offering me scholarships the opportunities to develop myself. Thank the Natural Science and Engineering Research Council of Canada for their financial support of this research.

Specially, thank my family for their love and support which I am eternally grateful, thanks to my love Runxuan who lighted up this dark, stressed thesis-writing winter.

I will always remember these wonderful two years, during which I felt struggling but become more mature and stronger; I meet wonderful people and spent memorable time with them; I feel my growth and found my interest. Hope I would keep the courage, passion, and curiosity to face upcoming adventure. Thanks to myself and wish me a bright future.

# Table of Contents

# List of Tables

# List of Pictures

# 1. Introduction

Due to the complexity of the human neural systems, its disorders are the most difficult disease to treat. Gratifiedly, due to the significant progress made in understanding the function and mechanism of nervous systems in recent years, neural disorders and injuries have become possible to treat by implanting neural prostheses. For examples: visual prostheses[3, 4], artificial cochlear[5], neural motor prostheses[6], deep-brain stimulators[7]. Furthermore, many studies in the past thirty years show people's intent can be transferred to the computer through brain-computer interfaces(BCI)[8], which is an exciting and motivating application worth of developing[9]. In these devices, the neural electrode or electrode arrays act as the intermedia of the communication between the electronic systems and the neural system. The electrodes could either excite the neurons, and those are so-called *stimulating electrodes,* or they can sense the neural signal, and those are so-called *recording electrodes*.

A successful neurons excitation happens only when enough charge is delivered from the electrode to extracellular liquid [2], while the size of stimulating electrodes is required to be as small as possible for minimum implant injury and high spatial resolution. Thus, the electrode materials are desired to provide a large charge density under a safe potential range. Many biocompatible materials are currently applied or showing potential to be used as stimulating electrodes, including metal and metal compounds, such as platinum[10], gold[11], iridium, iridium oxide, titanium nitride[12], tantalum/tantalum oxides[13, 14]; conducting polymers, like polypyrrole(PPy) and poly(3,4-ethylenedioxythiophene)(PEDOT)[15, 16]; graphene[17, 18]; and carbon nanotubes[19-21], among which iridium oxide attracts attention of researchers by showing outstanding faradaic charge injection[22], and it has been applied in commercial medical devices[23]. The performance of iridium oxide working as neural stimulating electrodes *in vitro* and *in vivo*, in terms of electrochemical properties,

biocompatibilities, stabilities, and stimulation protocols have been investigated thoroughly[3, 24-27]. Research focusing on further enhancing the performance by fabricating iridium oxide with rough surface area has been done[28]. However rough structures are found to degrade with time and to introduce porous impedance[2]. Recently, some researches have focused on mixing iridium oxide with other materials for neural stimulating electrode applications. Iridium oxides mixed with carbon nanotube, graphene oxides, PPy, and PEDOT are all showing better electrochemical properties than pure iridium oxide electrodes[29-31]. Another possible solution is mixing iridium oxide with other metal oxides, which is a common strategy applied in the field of supercapacitors which also demands electrode materials providing a high charge density[32].

Bismuth oxides drew our attention as a potential additive component because $Bi_2O_3$ films show a large capacitance as supercapacitor[32, 33] and good biocompatibility as a composition of dental root-end filling material.[34] Also, metallic $Ir_2Bi_2O_7$ has been reported having good conductivity and charge storage capacity.[35, 36]

However, the potential of using Ir-Bi mixed oxides as neural stimulating electrodes and the effect of Ir/Bi ratio on the resulting electrochemical properties have not yet been investigated. Thus, the research reported in this thesis investigated the influence of composition of $Ir_xBi_{1-x}$-oxide on the charge delivery of the material for a possible use as neural stimulating electrodes. Electrochemical properties, morphology, crystalline structure, stability, and biocompatibility of $Ir_xBi_{1-x}$-oxide ($x = 0, 0.2, 0.4, 0.6, 0.8$ and 1.0) coatings thermally deposited on a titanium substrate were investigated.

# 2. Background

## 2.1 Neural stimulating electrodes

The idea of using electrical stimulation for treatment of nervous disorder has a long history,[37] but it was not until last century that implantable neural prosthetics become a practical treatment of chronic neural disorder, which has been enabled due to the advanced understanding of the nerves system and technological innovations. Nowadays, neural stimulating electrodes are widely used in neuroscience research and employed in various prosthetic devices aiming to treat different neural disorders[9, 38], as several examples show in Figure 1.

### *2.1.1 Sensory prosthetics*

The cochlear implant, which was developed by William House in 1973 and used for restoration of hearing, is the first and the only FDA-approved sensory prosthetics. The state-of-the-art cochlear implant typically consist of 16 to 24 electrodes that stimulate the nerve fibers corresponding to different frequency of sounds (Figure1 (c))[39]. The success of cochlear implant is because of the surgically accessible anatomy of human cochlear, where electrodes could be easily placed close to auditory nerve, while the development of visual prosthetics (Figure1 (a)&(b)), and somatosensory prosthetics are hindered because complexity and surgically difficulty of the visual and the somatosensory neural system[40, 41].

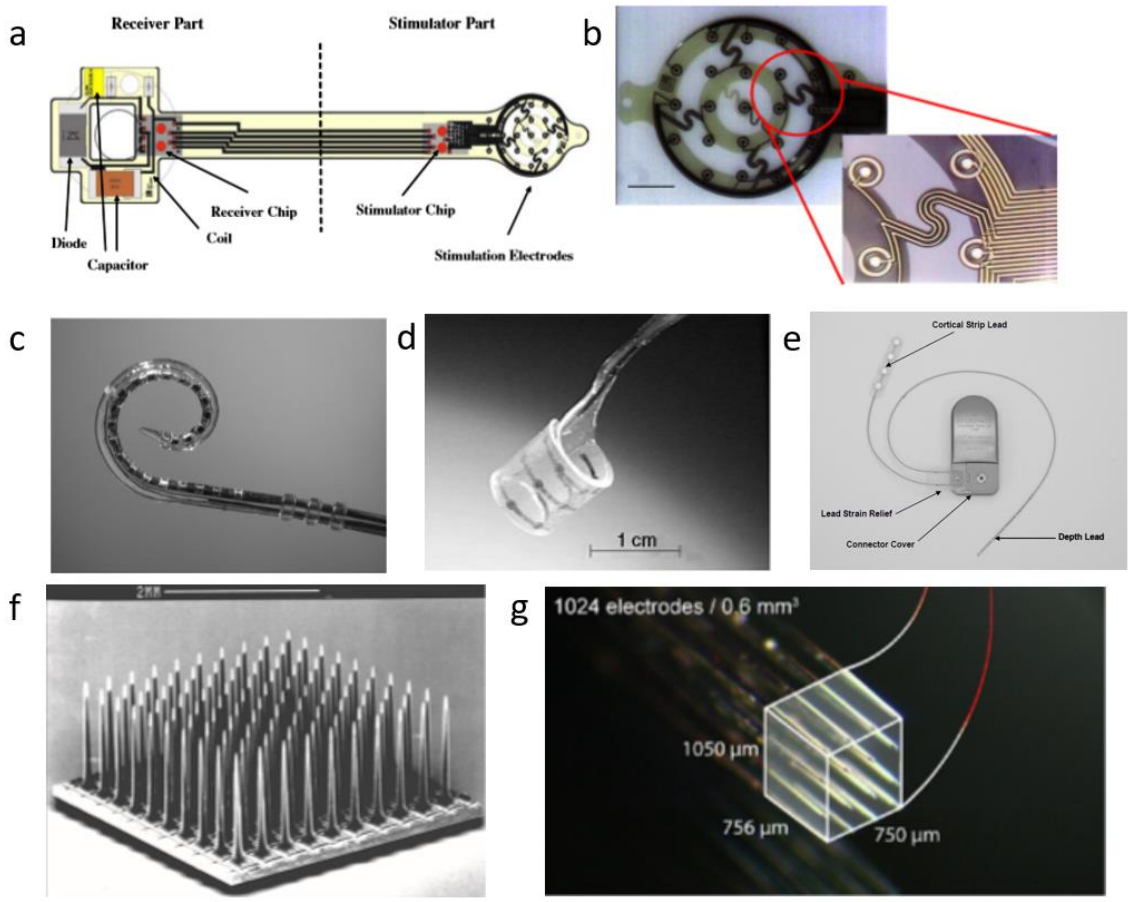


Figure 1. several examples of neural stimulating/recording electrodes. (a) Design of wireless epiretinal vision prosthesis. A flexible substrate with monolithic integration of interconnects and stimulating electrodes and hybrid assemble of electronic components. (b) micrograph of retinal stimulation array with 24 Pt electrodes [37]. (c) Cochlear Contour™ electrode arrays [38]. (d) cuff electrodes and cable for peripheral nerves stimulation [39]. (e) Neuropace RNS® System for seizures monitoring and controlling, with an implantable neurostimulator connected to two leads that placed into seizures onset areas [40]. (f) The Utah electrode array contains 100 penetrating microneedles, each 1.5 mm in length, that project out from a 4mm×4mm silicon substrate. The tips are deposited with Iridium oxide to facilitate electronic to ionic transduction. (g) high-density 3D gold electrode arrays used to obtain in vivo brain recording [41].

### 2.1.2 *Motor prosthetics*

Motor neural prosthetics are designed to rehabilitate neuromuscular function for patients who suffer from spin cord injury or some nerve diseases. Different from sensory prosthetics, which acquire external information, like sound and vision, the

motor prosthetics usually record the internal cognition of motion from skin surface electrodes [42, 43], or invasive intracortical electrodes arrays (Figure 1(f))[44]. Then, it analyses the signal and sends orders to the stimulation module to control the patient's limb or mechanical limbs. In the stimulation module of motor prosthetics, due to the lower neuron density and relative simplicity of the peripheral nervous system, invasive stimulating electrodes are not always required. For example, 'Parastep systems' applies skin surface stimulation to control lower limbs muscles[42]. However, the selectivity of skin surface electrodes is not enough to deal with a complicated system, so invasive electrodes are applied in complicated motion, like hand grasping [43, 45].

### *2.1.3 Neuromodulation*

Neural stimulating electrodes are also used for normalizing or modulating the disordered neural functions. Cardiac pacemaker is the most successful neuromodulation device, in which one or two electrodes are inserted into the right heart chamber(s) to stimulate the cardiac muscle helping control the heart rhythm. The successful application of pacemaker encouraged the development of implantable devices treating neural system disorder. Since the 1970s, deep brain stimulators with electrodes leading to subthalamic region or thalamus are used as chronic treatment of Parkinson's disease.[7, 46] Similarly, seizures caused by epilepsy could be treated with a set of recording electrodes and stimulating electrodes implanted at the location where seizures are generated (Figure 1.(e)). When an abnormal brain activity is detected, the stimulating electrodes that are controlled by a stimulator placed inside the skull, respond in real time to normalize the brainwaves[47]. Other FDA approved treatment include pain modulation by spinal cord stimulation, depression treatment by vagus nerve stimulation, and dystonia treatment and essential tremor by deep brain stimulation. Meanwhile, research and commercialization efforts are still focused on developing treatment of many other neural disorders like cluster headache and Tourette's disease.[40]

## 2.2 Stimulation mechanism

### *2.2.1 Physiological mechanism*

Although researchers found that there are numerous alternative methods of stimulating functional neurons response like magnetics, optogenetics, thermal, acoustic, or chemical stimulations[48], electrical neural stimulation is still the most mature technology and most widely applied in either neuroscience research or clinical practice of neural prosthetics. All these functions are achieved by generating or inhibiting the Action Potentials (APs), which are rapid rises and falls of transmembrane potential that are naturally triggered at the cell body and propagate the axon. At resting state, the extracellular potential is maintained at 60-80 mV higher than intracellular potential by the phospholipid bilayers membrane and the selective ion pumps across it (Figure 2 A). When a depolarization caused by either inner or outer ion flow reduces the transmembrane potential to a threshold, the voltage-sensitive sodium channel will open allowing $Na^+$ flow into the cell, further depolarizing the membrane (Figure 2. B). Then, potassium channels open, and $K^+$ ions flow out and repolarize the membrane. Last, ions concentration and transmembrane potentials are completely restored with $Na^+$ and $K^+$ transported back by ion pumps against the concentration gradient. During the opening of $Na^+$ and $K^+$ channels, ions also diffuse around inside the axon, depolarizing the surrounding membrane, so that the APs propagate along the axon.

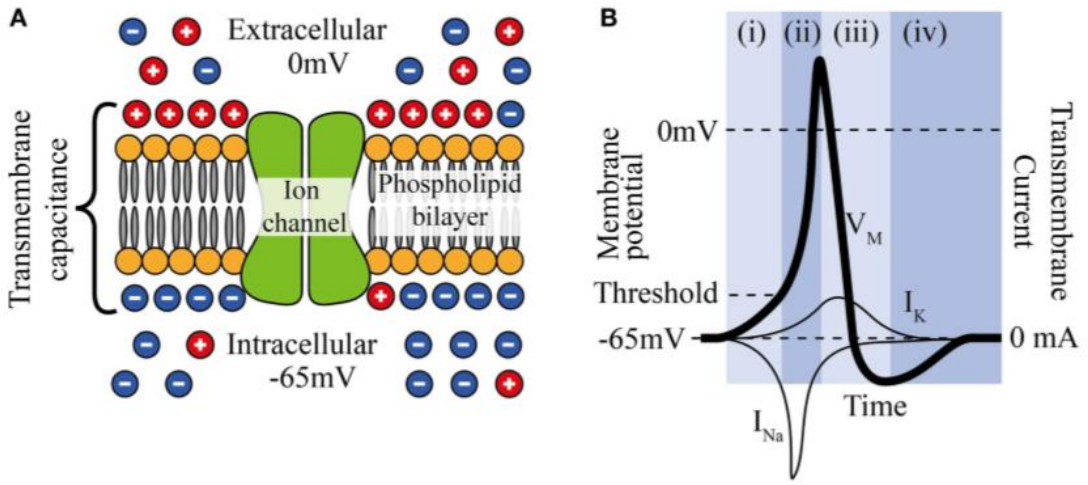


Figure 2. (A) The phospholipid cell membrane, ionic charges and an ion channel. (B) A typical action potential. (i) stimulation depolarizes membrane potential above threshold, (ii) Na+ channel opens and Na+ enters the cell causing a membrane potential increase, (iii) K+ channels are open and K+ leaves the cell, (iv) ion pump restore resting potential[48].

### 2.2.2 *Electrochemical mechanism(electrodes)*

Electrodes could be used to generate the initial depolarization either extracellularly or intracellularly by reducing the transmembrane potential to the threshold (Figure 2 B (i)), the neurons would finish the APs and transport the signal away by themselves as described above. Intracellular stimulating or recording is used in *in vitro* neuroscience research, providing high selectivity, instant response, and lower signal-noise ratio, but it damages the neuron's membrane and experiences difficulties in being applied on freely moving animals. Currently applicable neural prosthetics has one or serval working electrodes (WE) implanted very close to the target tissue to control transmembrane potential and excite neural signals extracellularly. Also, counter electrodes (CE) are needed to complete the stimulating circuit and are usually placed with a distance from stimulating electrodes[45].

## 2.3 Stimulating protocols

Usually, charge-balanced biphasic current pulse are applied on working electrodes, as shown in Figure 3(a) and (b), where the cathodal and anodal phase provide the same amount of opposite charges( $Q_c = i_c \times t_c = Q_a = i_a \times t_a$, where $Q$ is charge in Coulombs (C) and $t$ is time (in seconds)) to fully recover the electrochemical state of the electrodes before next pulse. Charge balance is very important because potential excursion because of accumulating of charge will induce irreversible faradaic reactions on tissue or electrodes[49].

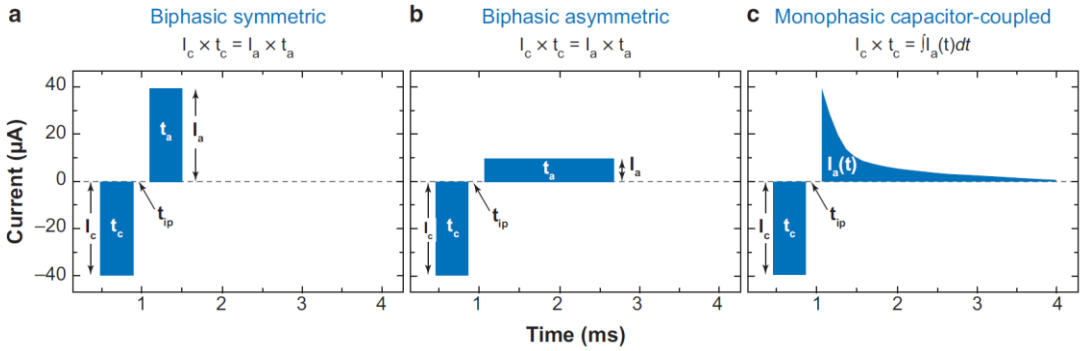


Figure 3. Biphasic symmetric, biphasic asymmetric, and monophasic capacitor-coupled waveforms for charge-balance stimulation[2]

The cathodal phase is generally used to stimulate neural response for physiologic reason. During the cathodal phase, the electrode potential is driven negative, so nearby positive ions are attracted to, and negative ions are forced away from the electrode. The ions flow drives the surrounding extracellular potential of neural membrane to negative so that the transmembrane potential reduces to the stimulating threshold, as shown in Figure 2B (i). The value of the threshold (minimum) current essential to stimulate the neurons can be determined using the following equation:

$$I_{th} = {}^{I_{rh}}/_{1 - \exp(-W/\tau_m)} \quad (1)$$

where $I_{th}$ is the threshold current(A); $I_{rh}$ (A) is the experimental minimum effective

current if the pulse width is very long; W is the pulse width (s), as $t_c$ in Figure 3; $\tau_m$ is the membrane constant (s).

The total charge essential to initiate an action potential, $Q_{th} = I_{th}W$, is found to increase with pulse width, which might be because of the redistribution of ions by diffusion so that not all charges reach the neurons before they diffuse away. Thus a narrow pulse width is desired to minimize the charge introduced to tissue[50, 51].

However, in real applications, the electrodes can hardly be attached to the neurons. Even worse, the neuron might move away from the electrodes, and the electrodes would be capsulated by glial cells because of the foreign body reaction[52]. Also, as the counter electrodes are sometimes placed with a distance from the stimulating electrodes, the electrical field close to stimulating electrodes is almost homogeneous, driving ions flows towards or away from the electrodes in all direction, so not all the charge accumulated to the electrode surface (Q in Figure3) can flow to the extracellular fluid near the target neurons.

Practically, the charge injection threshold is set up based on efficacy and safety concern, and it varies with materials, stimulation protocols, and target neuron types. For examples, for human penetrating deep brain stimulation, the threshold charge per phase is 135-400 $\mu C\ phase^{-1}$ with 60-200 $\mu s$ pulse width[53]; for human surface epiretinal vison prostheses, the threshold is 24-1000 $\mu C\ phase^{-1}$ with 2000 $\mu s$ pulse width[54].

## 2.4 Capacitive charge injection

Once the electrodes are inserted into the extracellular fluid, an electrical double layer will form because of the electrode potential, Figure 4. The first layer, next to the electrode, is the Helmholtz layer which consists of a plane of dipole molecules such as

water oriented at the electrode surface and ions specifically adsorbed on the electrode surface (inner Helmholtz layer), and an outer plane of hydrated ions and water molecules attracted to the surface because of electrical force (outer Helmholtz layer). The second layer is the diffusion layer, which also consists of hydrated ions but loosely distributed according to the Boltzman distribution. When external current or voltage is applied to the electrode, and there is no oxidation or reduction reaction happening, the double layer could be considered as a capacitor.

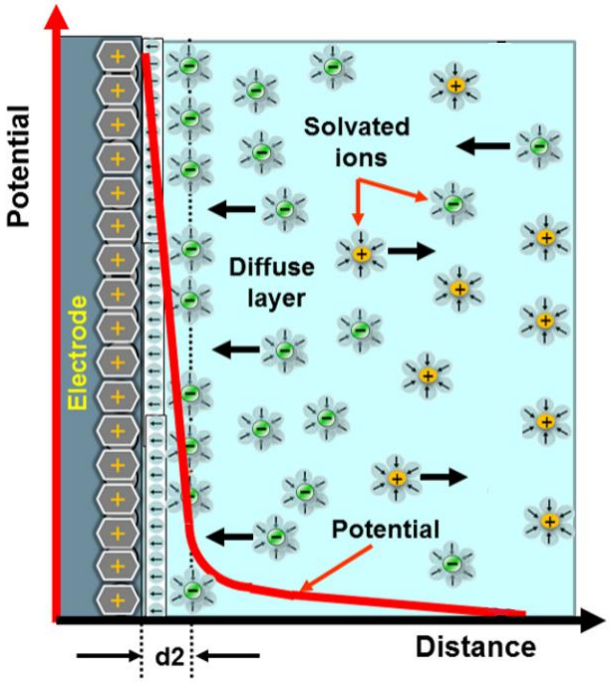


Figure 4. schematic of ions distribution and potential profile of capacitive double layer[1].

When the electrode potential is driven positively, as shown in Figure 4, more negative ions are attracted to the electrode surface, and positive ions are repelled. When the electrodes are driven negatively, the ions flow in the opposite direction. During the charging and discharging, the charges (ions) are delivered from electrode to extracellular electrolyte and flow to neurons without any electron transfer through the solid-liquid interface. This procedure is called capacitive charge injection, during which the amount of charge would be delivered to electrolyte would be described as:

$$\mathrm{Q} = \mathrm{C} \times \mathrm{V} = \frac{\varepsilon S}{d} \times V \quad (2)$$

where C is the capacitance (Coulomb/Volt, or F) of the double layer capacitor, V is the applied voltage (V), $\varepsilon$ is the permittivity of electrolyte in the double layer (F $m^{-1}$), $S$ is the surface area of the electrode-electrolyte interface ($m^2$), and $d$ is the characteristic separation distance of the double layer capacitor (m), which takes into account the presence of both the Helmholtz layer and the diffusion layer.

Titanium nitride and tantalum/tantalum oxide are ideal capacitive charge injection materials for neural stimulation, with high chemical stability and biocompatibility. However, their double layer capacitance per real surface area is generally small, and the voltage range is limited because of safety concern; considering equation (2), the total charge injection of a micro size electrode may not be enough to initiate an action potential [55]. High charge injection capacity can be obtained by fabricating a metal electrode with a high roughness, which has a significantly larger electrochemically active surface area (ESA) than its geometric surface area (GSA). Porous sputtered titanium nitride electrodes have been reported to have an *in vitro* charge injection capacity of 0.9 mC $cm^{-2}$[12].

## 2.5 Faradaic Charge Injection

The second charge injection mechanism is faradaic charge injection during which oxidation or reduction reactions happen at the electrode-tissue interface. Under stimulating current, usually cathodal, electrons accumulate at the electrode surface, as what also happens in the capacitive charge injection, until the electrode potential is driven to a threshold where reduction reaction occurs. The reduction reactions usually involve hydrogen ions absorption (intercalation) or hydroxide ions releasing from/to the electrolytes, which means charges are transferred through the electrode/electrolyte interface and during this the oxidative state of the metal changes. A faradaic reaction

provides an extra amount of charge, in addition to the capacitive charge injection, under the same conditions. The reactions should be completely reversible under the opposite pulse, since irreversible faradaic reactions like water electrolysis or electrode corrosion are harmful to the surrounding tissue. Also, the reactions should be occurring in the solid phase of the electrode, without bringing any new chemical species into the solution.

Platinum, iridium, or platinum iridium alloys are faradic charge injection materials that are commonly used in commercial neural stimulating electrode because of their high stability and biocompatibility. Platinum undergoes the following reduction and oxidation reaction during the processes of charging and discharging[26].

$$PtO + 2H^+ + 2e^- \leftrightarrow Pt + H_2O \quad (3)$$

and

$$Pt + H^+ + e^- \leftrightarrow Pt - H_{ads} \quad (4)$$

However, the faradaic charge injection provided by oxide formation from noble metals, such as Pt, is relevantly small comparing with noble metal oxides who usually have different oxide forms available for valence transition. Ir-oxides show outstandingly large charge injection capacity, low impedance, and biocompatibility, making it one of the most popular materials for neural stimulation and recording.[22, 56] During charging and discharging, the valance states of iridium switches between $Ir^{3+}$ and $Ir^{4+}$ as described by the equation:

$$2IrO_2 + 2H^+ + 2e^- \leftrightarrow Ir_2O_3 + H_2O \quad (5)$$

For safety concern, capacitive charge injection materials are better choices for neural stimulation than faradaic charge injection materials, because of their inert chemical activity[55]. However, TiN or $Ta/Ta_2O_5$, even with a porous morphology, are reported to have lower charge injection capacity than Ir-oxide[12].

## 2.6 Safety concern

The irreversible reaction may also occur at the electrodes when the electrode potential exceeded threshold values because of over-charging or the accumulation of unbalanced residue charges, which affects the stimulating efficiency and might release toxic ions into surrounding tissue.[55] Degradation of activated Ir-oxide film was observed after two days *in vivo* test with charge density about 3 mC/cm$^2$[26] and delamination was reported when the cathodic voltage exceeded -0.6 V versus Ag|AgCl[25]. Dissolution of Pt was observed at a charge density of 20-50 μC/cm$^2$[57] undergoing irreversible faradaic reaction when potential excursion exceeded a threshold value, as:

$$Pt + 4Cl^- \leftrightarrow [PtCl_4]^{2-} + 2e^- \quad (6)$$

Another irreversible reaction that may occur during neural stimulation is the electrolysis of tissue fluid. The water window is defined as the potential range between water electrolysis potentials, which depends on the materials of electrodes, as shown in Table 1. As water electrolysis usually happens before other irreversible reactions, the water window is set as the safe potential thresholds. Thus, the charge injection during the stimulating pulse is limited by the water electrolysis potential window.

Table 1. Water electrolysis potential windows of frequently used electrode materials

| Electrode material | Pt[57] | IrOx[58, 59] | TiN[12] | CNT[16] | PEDOT[15] |
|---|---|---|---|---|---|
| Water windows(V) Versus Ag\|AgCl | -0.6—0.8 | -0.6—0.8 | -0.9—0.9 | -1.5—1 | -1—0.6 |
| $Q_{(inj)}$ mC/cm$^2$ | 0.1-0.4 | 1-3 | 1 | 1-1.6 | 10 |
| Charge injection type | Faradaic | Faradaic | Capacitive | Capacitive | Faradaic |

## *2.7* Currently problems of NSEs and possible solutions

Currently, commercial neural prosthetics mentioned in Section 2.1 contain from one electrode (e.g. pacemaker) to multiple (array of) electrodes (e.g. cochlear implants). For neuromuscular stimulation or peripheral nervous system stimulation, a small number of electrodes is enough to repair the neuron function[40]. Also, because of the relevant lower neuron density and larger spatial space in peripheral nervous system, electrodes can have larger geometric size, like Figure 1(d) [60], so a lower charge injection density is needed to initiate functional neuron response, and the electrodes are less likely to degrade under stimulating current[2]. However, when dealing with the neural disease related to high nervous density area, high stimulating selectivity and high spatial resolution microelectrodes are required.

Although neural stimulating and recording electrodes share the same physiology and electrochemical principles in the opposite direction, reducing electrode sizes is a more difficult issue for stimulating electrode than recording electrodes. Modern electronic processing technology makes it possible to have 1024 recording electrodes in 0.6 $mm^3$(Figure.1(g))[61], and high-density brain recoding systems, like Michigan electrode arrays and Utah electrode arrays (Figure.1(f)), have already been applied in medical treatment for paralysis[62, 63]. However, for stimulating electrodes, as described by equation (2), when the size and surface area decrease, high charge injection capacity is required to ensure enough amount of charge is delivered to target neurons. Thus, biocompatible materials with large charge injection capacity and low impedance are worth to be investigated.

Pt and Ir-oxide are currently the most popular materials of neural stimulating electrode. A common practice to increase the charge injection is increasing the ESA/GSA ratio by either inducing rough surface or coating the materials on a porous substrate. Electrochemically modified Pt electrodes have reported showing about 75 times larger

real surface area than standard Pt electrodes[5]. Platinum black coating fabricated by current pulse electroplating in an ultrasonic bath, resulting in a 13 times larger charge storage capacity than a platinum electrode[10]. Different methods to increase the roughness of a silicon substrate before coating it with platinum were investigated, among which the platinum coating on a dry etched substrate gave a charge injection capacity of 0.50 $mC/cm^2$, comparing with 0.19 $mC/cm^2$ of an un-modified electrode, and the impedance of the substrate-modified coating decreased by 65%[64, 65]. Electrochemically deposited Pt on 800 nm length titanium nanotubes shown a large ESA and thus a ten times larger charge storage capacity than that of a sputtered Pt coating[66].

Ir-oxide films prepared through different methods have been investigated, with activated iridium oxide films (AIROF), electrodeposited iridium oxide films (EIROF), sputtered iridium oxide films (SIROF) or thermal deposited iridium oxide films (TIROF), exhibit similar magnitude of charge injection capacity[67, 68]. It has been reported that by changing the deposition rate of RF-sputtering, SIROF shows different morphology and the charge injection increased with a deposition rate increase[69]. Besides increasing the ESA/GSA ratio of Ir-oxide by changing deposition parameters, recent research to further enhance the performance has been focused on mixing Ir with other new promising materials.

Experience gained from research on electrochemical capacitors shows that mixture of noble metal oxides and other transition metal oxides may exhibit larger charge storage capacity than individual components at intermediate composition, which might be due to the lattice structure change because of the additive component allowing better ion penetration (intercalation) to deeper oxides layer[32, 70]. Ir-Ru oxides[71], Ir-Ni oxides[72], Ir-Ti oxides[73, 74] have been reported to yield the best electrochemical performance at Ir compositions of 80%, 20%, and 60%, respectively.

Conducting polymers, like polypyrrole(PPy), polyaniline(PANi), poly(3,4-ethylenedioxythiophene)(PEDOT), have been explored as good candidate materials for neural interfaces[75]. PEDOT with polystyrenesulfonate (PSS) dopant has shown a charge injection of 2.3 mC/cm$^2$, which is comparable with Ir-oxide, and their impedance was much lower than that of a thin film Pt electrode[76]. Other significant advantages of conducting polymers are that they can provide a softer interface between the metal electrode and serve as a scaffold for bioactive molecules such as anti-inflammatory factors, cell adhesion peptides, or growth factors, which could significantly enhance the neural attachment and biocompatibility[76]. However, electrodes based on electrically-conducting polymers lack stability (chemical, electrical and structural).

Carbon nanotubes (CNTs) is a promising capacity charge-injection material because of their naturally high ESA/GSA ratio and stable chemical and mechanical properties. Carbon nanotubes array were reported having a charge injection capacities of 1-1.6 $\mathrm{mC\ cm^{-2}}$, which is larger than Pt control but less than Ir-oxide control [21]. Besides, the high surface roughness of CNTs is excellent for neuronal cell adhesion[77]. CNTs can also act as high conductivity and high surface area substrates or skeletons for other materials. CNTs co-deposited with Ir-oxide[29], PEDOT[78, 79], and polypyrrole[80, 81] are all reported having larger charge injection capacity and lower impedance than their individual component.

# 3. Objective

As mentioned in section 2.7, further developing of neural prosthetics is obstructed by the trade-off between electrodes size and the amount of charge the electrodes can delivery to the neurons to excite action potentials. One of the solutions is developing electrode materials with large charge injection capacity so that the electrode could deliver a large amount of charge with a small geometric size.

The objective of this work is to explore whether Ir-Bi mixed oxide would be a promosing electrode for neural stimulation by achieving large charge injection capacity and low impedance to resolve the trade-off. Step by step sub-objective of this research includes:

1) To fabricate $Ir_xBi_{1-x}$-oxide (x=0, 0.2, 0.4, 0.6, 0.8, 1) on Ti substrates, and find the best ratio of Ir/Bi.
2) To investigate the morphology, crystal structure, chemical valance state of the mixed metal oxides.
3) To evaluate the stability and biocompatibility of the most promosing composition as a potential candidate of neural stimulating electrodes.

# 4. Experimental and Methods：

## 4.1 Sample preparation

$Ir_xBi_{(1-x)}$-oxide coatings (x=0, 0.2, 0,4, 0.6, 0.8, 1.0; x is the molar ratio in mol/mol, referring to the content of pure Ir in the precursor solution) were deposited on titanium substrates employing a thermal decomposition method. The round (button-shaped) titanium substrates, with a thickness of 2 mm, were cut from a Ti rod with a diameter of 1.27 cm (Macmaster Ultra-Corrosion-Resistant Grade 2 Titanium Rods). The Ti substrates were first wet polished using 400-grit SiC sandpaper. Next, four polished substrates were rinsed thoroughly and sonicated for 15 mins in isopropanol (purity 99.9 %, Fisher Scientific A416-1). Then, they were rinsed thoroughly and transferred to a boiling solution of hydrochloric acid (37 wt%, Fisher Scientific, Canada) and deionized water (1:1 by volume) for 30 min. After etching, the substrates were again thoroughly rinsed with deionized water, and dried with argon gas (MEGS Specialty Gases Inc., 99.998 wt% pure, Canada).

The stock precursor solutions were prepared from 0.1 mol/L $IrCl_3 \times 3H_2O$ (53%-56% Ir, Acros Organics 195500050) and 0.1 mol/L $BiCl_3$ (purity 98+%, Acros Organics 208830250) dissolved in the solution of hydrochloric acid (37 wt%, Fisher Scientific, Canada) and deionized water (resistivity 18.2 MΩ cm), 1:1 by volume. The dried Ti substrates were put into a Teflon holder with four holes with the same diameter as Ti substrates to make sure the precursor solution does not spill out over the button side. The precursor solution of Ir and Bi salts were mixed in the desired ratio of x:1-x (x=0, 0.2, 0,4, 0.6, 0.8, 1.0) by volume, then a volume of 15 μl of the precursor solution was pipetted on the substrate. The solution dispersed uniformly and naturally because of the hydrophilicity of the etched Ti substrate. Then, the substrates with the Teflon holder was transferred into an oven at 358K for solvent evaporation. After 10 mins, the Teflon

holder was removed, and the substrates were transferred into an air-natural-convection furnace at 773K for 15 mins. After this, the samples were removed from the furnace and cooled down to room temperature, and then the second layer of 10 μl precursor solution was pipetted on the surface, following by drying in the oven for 5 mins and annealing in the furnace for 15 mins. This procedure was repeated four times, with totally five coating layers formed on the Ti substrate. At the end of the last cycle, the substrates were placed in the furnace at 773K for one hour to complete the oxidation of the $Ir_xBi_{1-x}$-oxides coating.

## 4.2 Surface/chemical/structural characterization

The surface topography and chemical composition of the $Ir_xBi_{(1-x)}$-oxides coatings were investigated using scanning electron microscopy (SEM) and energy-dispersive X-ray spectroscopy (EDS) analysis (instrument: Hitachi SU-3500 Variable Pressure SEM/EDS detectors). The surface chemical states and compositions of metal-oxide coatings were investigated using X-ray photoelectron spectroscopy (XPS) (Thermo Scientific K Alpha XPS instrument). The samples were first ion-beam etched before performing XPS. The crystal structure of the coatings was determined by X-ray diffraction (XRD) (Bruker D8 Discovery X-Ray Diffractometer).

## 4.3 Electrochemical Characterization

All electrochemical measurements were carried out using a three-electrode electrochemical cell, comprised of a saturated calomel reference electrode (RE), a graphite counter electrode (CE), and $Ir_xBi_{1-x}$-oxides samples as the working electrode (WE). A Teflon holder that exposes 1 $cm^2$ of the sample area to the electrolyte was used to hold the working electrode. Phosphate buffer saline (PBS) made of 0.137M NaCl (purity 100%, Thermal Fisher 177082) + 0.0027M KCl (purity ≥99% Fluka Chimika, 60132) + 0.01M $Na_2HPO_4$ (purity, Thermal Fisher, 105895) + 0.0018M $KH_2PO_4$ (purity 99%, Thermal Fisher LOT 153974) at pH 7.4 was used as the physiological simulating

electrolyte. The electrolyte was deoxygenated by continuous Ar gas purging for 20 mins before each testing. The electrodes were connected to a potentiostat (Autolab PGSTAT30, Metrohm, NL) driven by software NOVA (V2.0 Metrohm, NL). The electrochemical testing system is showing as Figure 5.

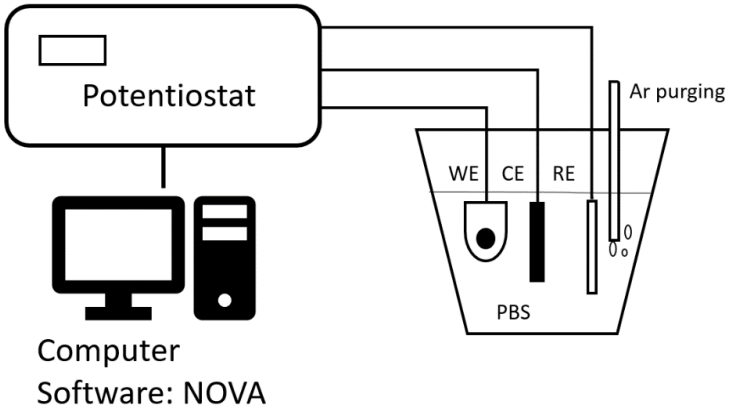


Figure 5. Schematic illustration of three electrodes electrochemical measurement system.

The water window and redox behaviors of $Ir_xBi_{1-x}$-oxide were first evaluated using cyclic voltammetry (CV) at a scan rate of 10 mV/s from -1V to 1V (SCE). Charge storage capacity (CSC) of all Ir-Bi oxides compositions as a predictor of charge injection capacity (CIC)[2] were measured from cyclic voltammetry (CV) at a scan rate of 50 mV/s from -0.6 V to 0.8V (SCE). The impedance of the electrodes was evaluated using electrochemical impedance spectroscopy (EIS) scanning at 0V(SCE) from 0.1 Hz to $10^5$ Hz after 20 cycles of CV charge storage capacity test.

Long-term stability of as-prepared Ir-oxide, $Ir_{0.8}Bi_{0.2}$-oxides electrodes were evaluated by running 2000 cycles of CV at a scan rate of 50 mV/s from -0.6 V to 0.8V (SCE). EIS tests were performed before and after the long-term CV test. Then, 5ml out of totally 80 ml 0.1 M PBS electrolyte after each running was analyzed with inductively coupled plasma (ICP, Thermo Scientific, iCAP 6000 series ICP spectrometer) to determine dissolved metal elements in the solution.

The electrochemically active surface area (ESA) of each sample composition was determined by performing CV at different scan rates in a solution of 2 mM potassium ferricyanide [$K_3Fe(CN)_6$] (purity 99%, SIGMA-ALDORICH, 063K3627) in 0.1 M potassium nitrate [$KNO_3$] (purity≥ 99.0% SIGMA-ALDORICH, MKBW5086V). The ESA would be calculated from Randle-Sevcik relationship

$$I_p = kn^{3/2}AD^{0.5}C_b v^{0.5} \quad (7)$$

where k = 268; n is the number of electrons transferred per molecule of ferricyanide; A is the area of the electrode in $cm^2$; D is the diffusion coefficient in $cm^2/s$; $C_b$ is the solution concentration in mol/L; and ν is the scan rate of the potential in V/s. In these measurements, the reduction peak current ($I_p$ in A) was measured and its dependence on $\nu^{1/2}$ was plotted, and then from the slope of the behavior, A was calculated.

## 4.4 Immunocytochemistry

The immunocytochemistry tests were performed in collaboration with Dr. Heather Durham's Neurotoxicology group (Montreal Neurological Institute and Hospital). The electrode samples to be studied (Ir oxide, and $Ir_{0.8}Bi_{0.2}$-oxides) were first rinsed and sterilized with ethanol (95%). Then, they were placed into a 24-wells dish, where cover glass (18MM GRWTH Thermofisher, 1254584) coated with poly-d-lysine (Sigma P7280) and Matrigel (Millipore B354234) were pre-placed in each well. Primary cultures of dissociated spinal cord (along with dorsal root ganglia) were prepared from embryonic day 13 (E13) CD1 mouse embryos(Charles River, St. Constant, Quebec), following a protocol approved by the McGill University Animal Care Committee [82]. The cells were plated on the top of electrode samples in each well at a density of 475000 cells/well and kept at 37°C until 40 DIV when cell survival was quantified.

After 40 DIV, the samples were removed from the culture wells, and cells were fixed with 4% paraformaldehyde in PBS at room temperature for 10 min. After washing with

PBS, the cells were permeabilized with 0.5% nonyl phenoxypolyethoxylethanol (NP 40) in PBS for 1 min. The permeabilized cells were submerged in 4% PFA for another 2 min, then they were submerged in 5% horse serum (InVitrogen 16050-015) in PBS for 30 min. The cells were then incubated for 30 min with rabbit Anti-Neurofilament H (200 kDa) Antibody (1:300, Chemicon AB1989) and mouse TuJ-1(1:300, neuron-specific class III β -tubulin, Neuromics MO15013), followed by three times rinsing with PBS. Then, the cells were incubated with two secondary antibodies, Cy™3 AffiniPure Donkey Anti-Rabbit IgG (H+L) (1:300, Jackson ImmunoResearch, 711165152) and Alexa Fluor® 488 Donkey Anti-Mouse IgG (H+L), (1:300, Jackson ImmunoResearch, 715545150) for 30 min, followed by 3 times rinsing with PBS. Last, the cells were mounted with ProLong™ Gold Antifade Mountant with DAPI (ThermoFisher Scientific P36931). Photographs were taken using Zeiss Observer Z1 microscope (Carl Zeiss Canada Ltd, Toronto, ON, Canada), equipped with a Hamamatsu ORCA-ER cooled CD camera (Hamamatsu, Japan). Images were acquired under 100x magnification and analyzed with Zeiss Axiovision software. Three radial fields were systematically taken with each sample for cell counting.

# 5. Result and discussion

## 5.1 Surface morphology/topography

The surface morphologies of $Ir_xBi_{(1-x)}$-oxides coatings were investigated using scanning electron microscopy (SEM). The electrode morphology was found to change with composition, Figure 6. The Ir-oxide coating shows a hills-like rough surface, while $Ir_{80}Bi_{20}$-oxides coating is flatter with a typical thermal deposition "cracked-mud" morphology and lower porosity[83]. When Ir composition decreased to 20% (Figure 6. (c)), a flower-like crystal structure shows up, which is consisting of pieces of crystallites like the petals of the flower. Energy-dispersive X-ray spectroscopy (EDS) shows that when Ir content is large than 40%, Ir and Bi exhibits a uniform surface distribution. The flower structure in $Ir_{0.2}Bi_{0.8}$-oxide was confirmed to have abundance of Bi. EDS shows that the flowers area, spots 2&3 in Figure 6. (f), shows a Bi content larger than 75%, while on the bulk surface, spots 1&8 in Figure 6. (f), the Bi content is 45% and 60%, respectively. A similar flower-like structure is also present on the pure Bi-oxide coating surface and in literature[84], which is predicted to be crystalline of abundant Bi-oxide, Figure 6 (g&h).

The surface chemical compositions of electrode coatings was investigated using EDS mapping and XPS, as shown in Table 2. The table shows that the composition obtained by EDS is slightly different for certain coatings with respect to the precursor solution composition, and the same is true for XPS results (to be discussed further down in the thesis). The difference might be either due to the nonhomogeneous distribution of Bi and Ir through the coating depth (the depth probing range of EDS is ca. 2 μm and that of XPS is ca. 5 nm) or due to the lower solubility of the Ir precursor salt, which might have resulted in the transfer of solid (non-dissolved) $IrCl_3$ crystals on the Ti surface, thus resulting in a higher Ir content than desired.

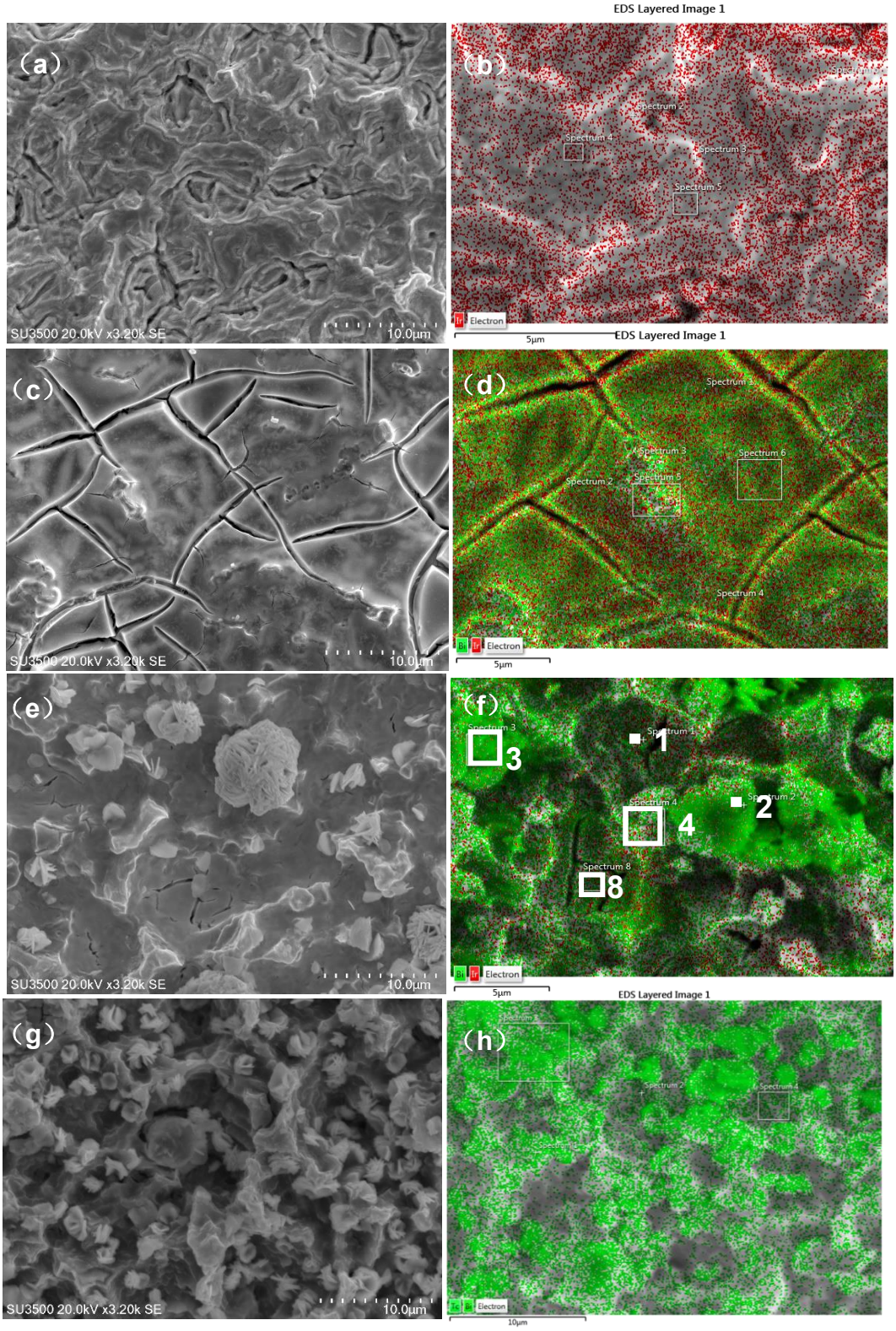


Figure 6. SEM and EDS of Ir-oxide (a & b), $Ir_{0.8}Bi_{0.2}$-oxide (c & d), $Ir_{0.2}Bi_{0.8}$-oxide (e & f), Bi-oxide (g & f). In EDS mapping, Ir is labelled in red and Bi is labelled in green.

*scale bar is not uniform in Figure (b & d & f & h)

**the presence of Tc in green in (f) is misinterpretation of Bi

Table 2. Molar percentage of Ir in $Ir_xBi_{1-x}$-oxide coatings. Nominal values refer to Ir content in metal precursor salt.

| Element content | | |
|---|---|---|
| Nominal* | Ir content from EDS % | Ir content from XPS %** |
| IrOx | 100% | 100% |
| $Ir_{0.8}Bi_{0.2}$-Oxides | 79.9% | 60% |
| $Ir_{0.6}Bi_{0.4}$-Oxides | 75% | |
| $Ir_{0.4}Bi_{0.6}$-Oxides | 60.0% | |
| $Ir_{0.2}Bi_{0.8}$-Oxides | 28.0% | 29% |
| BiOx | 0% | |

*Nominal composition is used in the following discussion.

** Only Ir-oxides, $Ir_{0.8}Bi_{0.2}$-Oxides, and $Ir_{0.2}Bi_{0.8}$-Oxides were tested.

## 5.2 X-ray photoelectron spectroscopy (XPS)

Figure 7 shows high-resolution XPS spectra of Ir and Bi for desired $Ir_xBi_{1-x}$-oxide compositions. The spectra were deconvoluted and the corresponding atomic ratio (AR) of each element was calculated and reported in Table 2.

The asymmetric 4f bands of Ir indicated that multi oxidation states exist, and the 4f 5/2 and 4f 7/2 Ir bands of Ir-oxides, $Ir_{0.8}Bi_{0.2}$ -Oxides, and $Ir_{0.2}Bi_{0.8}$-Oxides were all resolved into three pairs of doublets. Each doublet has two peaks with same FWHM, an area ratio of 4:3, and~ 3 eV gap in between, as seen Figure 7.

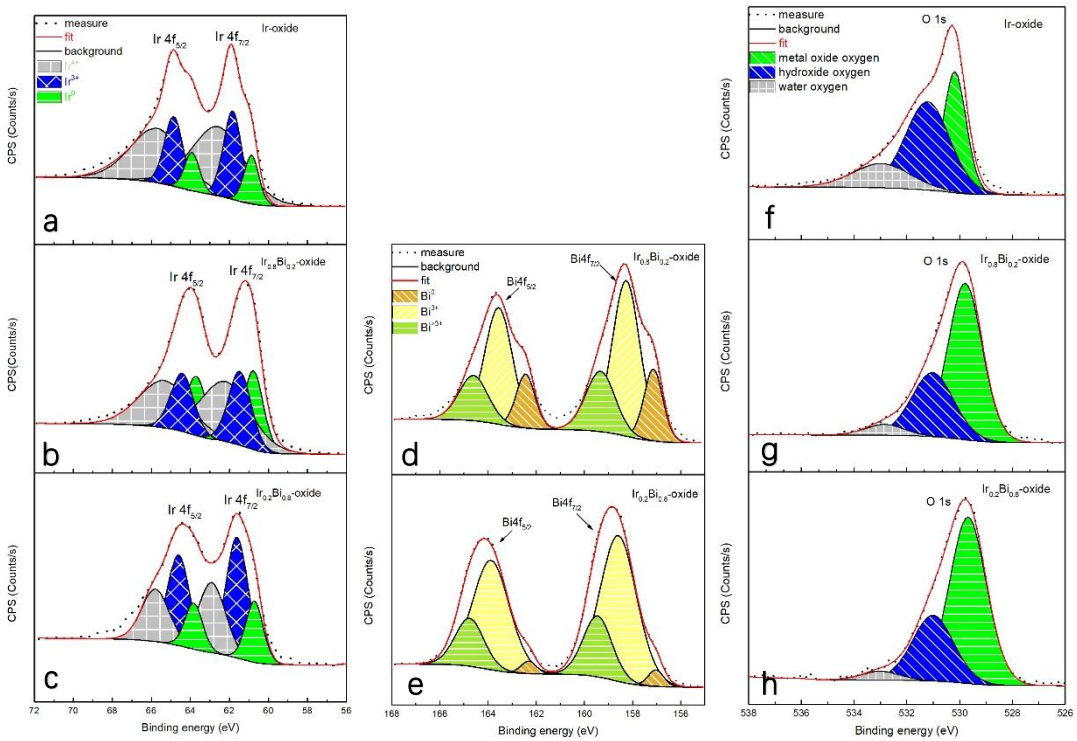


Figure 7. Fitting of XPS spectra. (a) Ir spectra in Ir-oxide; (b) Ir spectra in $Ir_{0.8}Bi_{0.2}$-oxide; (c) Ir spectra in $Ir_{0.2}Bi_{08}$-oxide; (d) Bi spectra in $Ir_{0.8}Bi_{0.2}$-oxide; (e) Bi spectra in $Ir_{0.2}Bi_{08}$-oxide; (f) O spectra in Ir-oxide; (g) O spectra in $Ir_{0.8}Bi_{0.2}$-oxide; (h) O spectra in $Ir_{0.2}Bi_{08}$-oxide.

The three doublet peaks of different composition were found located at the same position, as shown in Table 3. The lowest doublet was found located at 60.7±0.1 eV and 63.8 ±0.1 eV, which are agreement with the bonding energy (BE) of Ir metal[85, 86]. The presence of metal is possibly resulting from 'disproportionation' of lower-oxidative-state Ir oxides into metallic Ir and higher-oxidative-state Ir-oxide during annealing [87], or from the reduction of oxides during electrochemical tests. The BE doublet peaks at around 61.6 eV and 64.6 eV refer to Ir at the valence state of III, and the doublets of Ir at valence state of IV was found at ~62.7 eV and 65.7 eV. It is noticed in Table 3 that $Ir^{3+}$ is the main valence state of Ir in $Ir_{0.8}Bi_{0.2}$-oxide and $Ir_{0.2}Bi_{0.8}$-oxide, with almost a 50% contribution, while in pure Ir-oxide, the major part of Ir stays at valance $Ir^{4+}$, where $IrO_2$ is supposed to form.

Table 3. Fit data of Ir from XPS spectra.

| | $Ir^0$ | | | $Ir^{3+}$ | | | $Ir^{4+}$ | | |
|---|---|---|---|---|---|---|---|---|---|
| | B.E. | | A.R. | B.E. | | A.R. | B.E. | | A.R. |
| | 4f 5/2 | 4f7/2 | | 4f 5/2 | 4f 7/2 | | 4f 5/2 | 4f 7/2 | |
| Ir-oxide | 63.9 | 60.9 | 12% | 64.9 | 61.8 | 27% | 65.7 | 62.6 | 61% |
| $Ir_{0.8}Bi_{0.2}ox$ | 63.7 | 60.8 | 25% | 64.4 | 61.5 | 49% | 65.3 | 62.2 | 26% |
| $Ir_{0.2}Bi_{0.8}ox$ | 63.8 | 60.7 | 19% | 64.6 | 61.6 | 47% | 65.8 | 62.9 | 34% |
| ref[85, 87] | 63.8 | 60.8 | | 64.6 | 61.6 | | 65.7 | 62.7 | |

The bismuth 4f spectra were also resolved into three pairs of doublets but with a gap ~5.3 eV in between, as seen in Figure 7 [88]. A small amount of Bi is found in the pure metal state whose 4f 7/2 peak is shown at ~157.0 eV. The major part of Bi is present in the $Bi^{3+}$ oxidation state. Two other small peaks at BE ~1 eV higher than $Bi^{3+}$ are possibly corresponding to Bi at a higher oxidation state or belong to satellite peaks of $Bi^{3+}$.

Table 4. Fit data of Bi from XPS spectra.

| | $Bi^0$ | | | $Bi^{3+}$ | | | $Bi^{x+}$ x>3 | | |
|---|---|---|---|---|---|---|---|---|---|
| | B.E. | | A.R. | B.E. | | A.R. | B.E. | | A.R. |
| | 4f 5/2 | 4f7/2 | | 4f 5/2 | 4f 7/2 | | 4f 5/2 | 4f 7/2 | |
| $Ir_{0.8}Bi_{0.2}ox$ | 162.4 | 157.1 | 18% | 163.6 | 158.3 | 58% | 164.6 | 159.3 | 24% |
| $Ir_{0.2}Bi_{0.2}ox$ | 162.3 | 157.0 | 3% | 163.9 | 158.6 | 73% | 164.8 | 159.5 | 24% |
| ref[33, 88] | 162.2 | 156.9 | | 163.9 | 158.6 | | | | |

The oxygen spectra in Ir-oxide, $Ir_{0.8}Bi_{0.2}$-oxide, $Ir_{0.2}Bi_{0.8}$-oxide ware all resolved to three peaks as shown in Figure 7 f-h. The first peak at ~530.0±0.2 eV refers to the oxygen in metal oxides. A slight right shift when Ir percentage decrease might result from the lower Bi-O bonding energy comparing with Ir-O bonding energy [89]. The second peak at ~531.1±0.1 eV corresponds to metal hydroxide, and the third peak at

~533±0.1 eV is predicted from the oxygen atom of water[90]. It is noticed that in Ir-oxide, 49% percentage of oxygen is forming hydroxide, while in the Ir-Bi oxide, the major form of oxygen is metal oxide oxygen.

Table 5. Fit data of oxygen from XPS spectra.

| | Metal oxide | | hydroxide | | water | |
|---|---|---|---|---|---|---|
| | B.E. | A.R. | B.E. | A.R. | B.E. | A.R. |
| Ir-oxide | 530.2 | 34% | 531.2 | 49% | 533 | 17% |
| $Ir_{0.8}Bi_{0.2}ox$ | 529.8 | 63% | 531.0 | 32% | 532.9 | 5% |
| $Ir_{0.2}Bi_{0.8}ox$ | 529.7 | 67% | 531.0 | 30% | 533 | 3% |

## 5.3 X-ray diffraction

The crystallographic structure of the Ir-oxide, $Ir_{0.8}Bi_{0.2}$-oxide, $Ir_{0.2}Bi_{0.8}$-Oxides was investigated using X-ray diffraction (XRD), and the spectra are shown in Figure 8. A strong background of Ti and Ti-oxide from the substrate is observed[71, 90]. Rutile structure $IrO_2$ is found in the pattern of Ir-oxide coating[71, 86], which corresponds to the high ratio of $Ir^{4+}$ oxidation state from XPS result in Table 3. In the spectra of $Ir_{0.8}Bi_{0.2}$-oxide and $Ir_{0.2}Bi_{0.8}$-oxide coatings, small peaks of Ir-oxide are found at 2θ equals to ~53 and 70 degree. In the spectra of $Ir_{0.2}Bi_{0.8}$-oxide, the very small peaks at ~33 degree and ~42 degree might come from Bi-oxide we found in SEM imagine[84]. Peaks shift to right when bismuth content increase, which might because when Bi atoms replaced Ir of Ti atom in their rutile structure the lattice constant increases as Bi-O bond is longer than Ir-O bond and Ti-O bond.

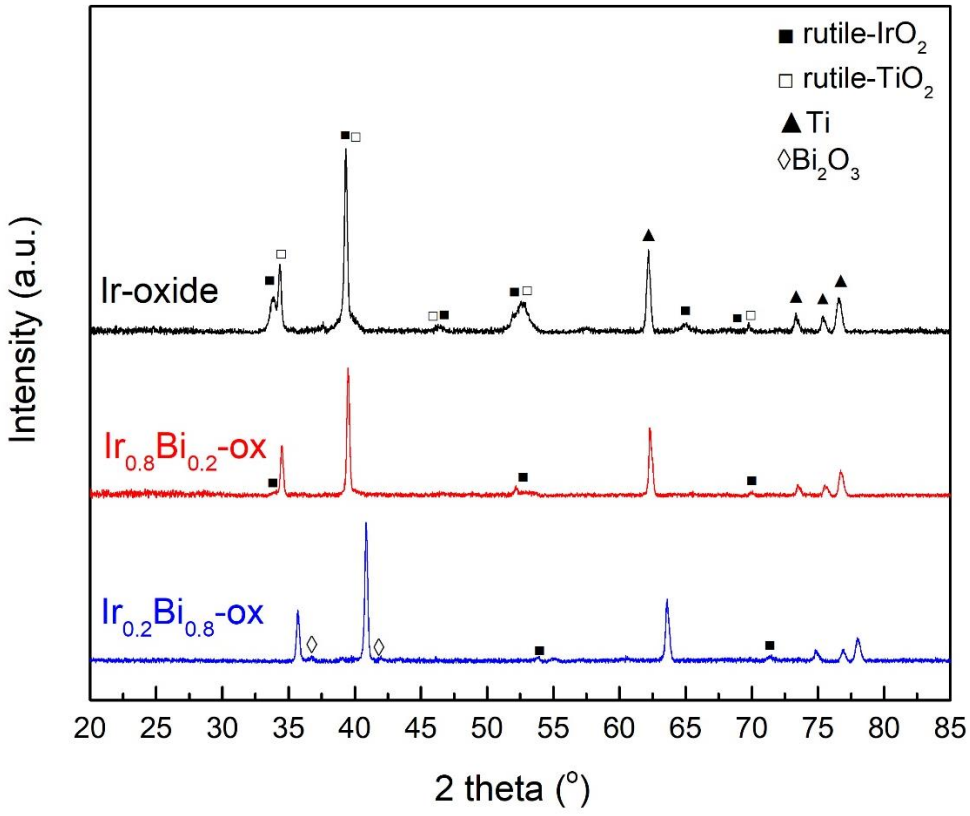


Figure 8. X-ray diffraction (XRD) patterns of Ir-oxide, $Ir_{0.8}Bi_{0.2}$-oxide, $Ir_{0.2}Bi_{0.8}$-oxide.

## 5.4 Electrochemical measurements

### *5.4.1 Redox behavior and water window*

The redox behavior of mixed metal oxide electrodes was investigated with CV under slow scanning rate, where the faradaic reaction would result in a clear peak since at slow scanning rate, the redox species have enough time responding to the potential change and providing extra faradaic charge[55].

The CV plots of Ir-oxide, $Ir_{0.8}Bi_{20}$-oxide, $Ir_{0.2}Bi_{0.8}$-oxide were shown in Figure 9. The thermally-deposited mixed metal oxide coatings produced in this work exhibited a slightly wider water window (ca. 1.6 V, i.e. from -0.8 V to 0.8 V vs. SCE) than the water window of Ir-oxide electrodes used for neural stimulation employed by other authors, which is from ca. -0.64 V to 0.76 V vs SCE (1.4 V)[58, 59].

From Figure 9, notable reduction peaks of Ir are shown at ~-0.4 V that would be associated to the reduction from Ir (III) to lower valence state, and a reduction plateau at ~0.3V could be attributed to reduction from Ir (IV) to Ir (III)[91]. The corresponding broad oxidation wave could also be observed at ~0.2 V. The two redox peak of Bi would also be confirmed by comparing with literature [33], where the two reduction peaks and two corresponding oxidation peaks can be attributed to two steps redox between Bi metal and $Bi_2O_3$.

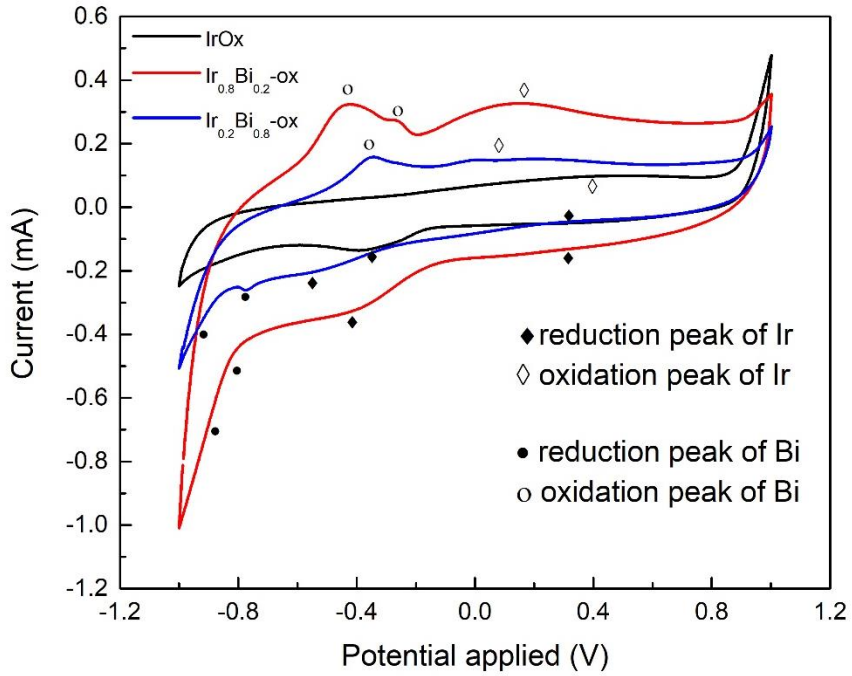


Figure 9. CV plots of Ir-oxide; $Ir_{0.8}Bi_{0.2}$-oxide, $Ir_{0.2}Bi_{0.8}$-oxide recorded at a scan rate of 10 mV/s in PBS solution.

In conclusion, the CVs in Figure 9 indicate that the investigated coatings could potentially be used for charge storage/delivery through redox reactions.

.

### 5.4.2 *Charge storage capacity*

Charge storage capacity (CSC), as a predictor of charge injection capacity, was determined using cyclic voltammetry (CV) in 0.1M PBS, within the voltage range of -0.6 V to 0.8 V(SCE) and at a scan rate of 50 mV/s. The specified voltage range (1.4 V) was set to be narrower than the one in Figure 9 because the same voltage range (1.4 V) is used in literature on Ir-oxide neural electrodes, and enables compression of our results to those in the literature[27, 59]. The CSC in cathode phase ($mC/cm^{-2}$), which present the charge that could be delivered by the electrode to the surrounding tissue within the specified potential limit, is usually considered and could be calculated from:

$$\mathrm{CSC}_c = (\frac{1}{v}\int_{-0.6}^{0.8} |i_c| dE)/A \tag{8}$$

where E(V) is the potential applied between WE and RE, $i_c$ is the measured cathodic current (mA), $v$ is the scan rate (mV/s), and A is the GSA ($cm^2$).

Figure 10 shows the CVs of Ir-oxide, $Ir_{0.8}Bi_{0.2}$-oxide, $Ir_{0.2}Bi_{0.8}$-oxide electrodes at the $20^{th}$ cycle. The mean $CSC_c$ per GSA of Ir-oxide was 4.6 $mC/cm^2$ with a standard deviation of 0.6 $mC/cm^2$, which is in the same magnitude of Ir-oxide macroelectrodes reported elsewhere[58, 69, 71, 72]. However, this value is not comparable to $CSC_c$ of a microelectrode which usually has larger $CSC_c$ per GSA because of different diffusion/intercalation behavior at the two different spatial scales[69, 92]. For example, The $CSC_c$ of sputtered Ir-oxide was reported decreasing with an increase in GSA [24]. The $CSC_c$ per GSA significantly increased to 17.7 $mC/cm^2$ when adding 20% Bi to pure Ir-oxide, while further increase in Bi to 80% resulted in a decrease of $CSC_c$ to 8.3 $mC/cm^2$ (Figure 10).

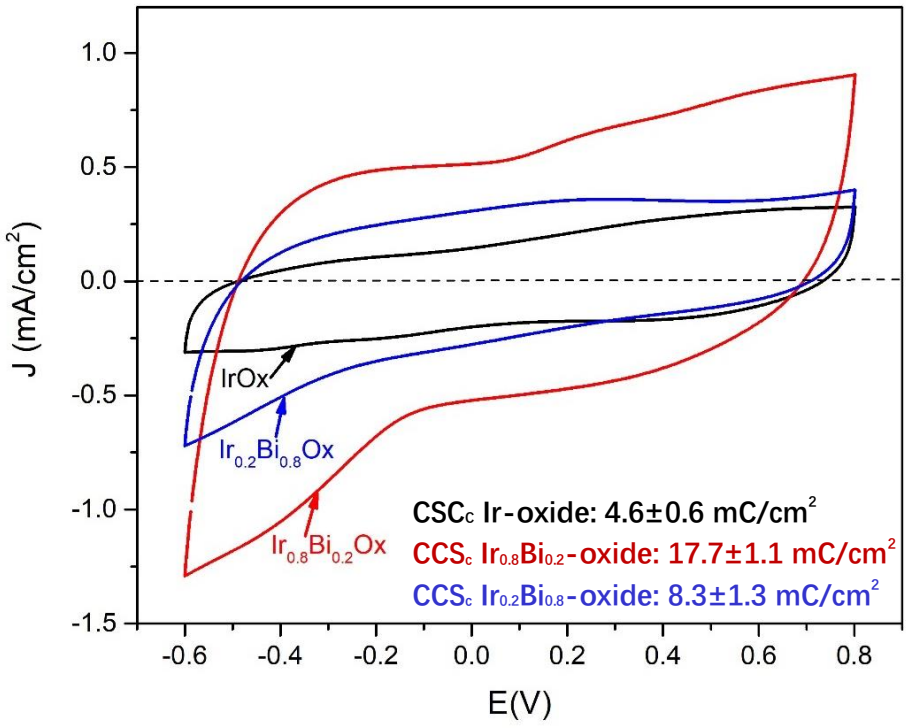


Figure 10. CV plots of IrOx (black), $Ir_{0.8}Bi_{0.2}$-oxide (red), and $Ir_{0.2}Bi_{0.8}$-oxide (blue) recorded in PBS at a scan rate of 50 mV/s in 0.1M PBS solution.

To better see the effect of $Ir_xBi_{(1-x)}$-oxide composition on the resulting $CSC_c$, results obtained by CV are summarized in Figure 11. This plot shows the $CSC_c$ expressed with respect to both geometric surface area (GSA) and electrochemically active surface area (ESA), the latter being determined employing equation (7) (for details related to ESA determination, see Appendix(A)). The trend in Figure 11 is the same for both GSA and ESA values. $Ir_{0.8}Bi_{0.2}$-oxide yields the largest $CSC_c$ (26.8mC/cm$^2$) among the compositions studied. When comparing to the current state-of-the-art, Ir-oxide, the increase in CSCc (based on ESA) for the $Ir_{0.8}Bi_{0.2}$-oxide is five-fold. As the stoichiometric number of charges involved in the redox transitions in the oxide phase of Ir-oxide and Bi-oxide are not significantly different, it is suggested that the five-fold larger faradaic charge injection of $Ir_{0.8}Bi_{0.2}$-oxide could be attributed to the mixed oxide structure allowing ions transfer to the inner oxide layer so that more oxide species are involved in the faradaic charge injection[33, 55].

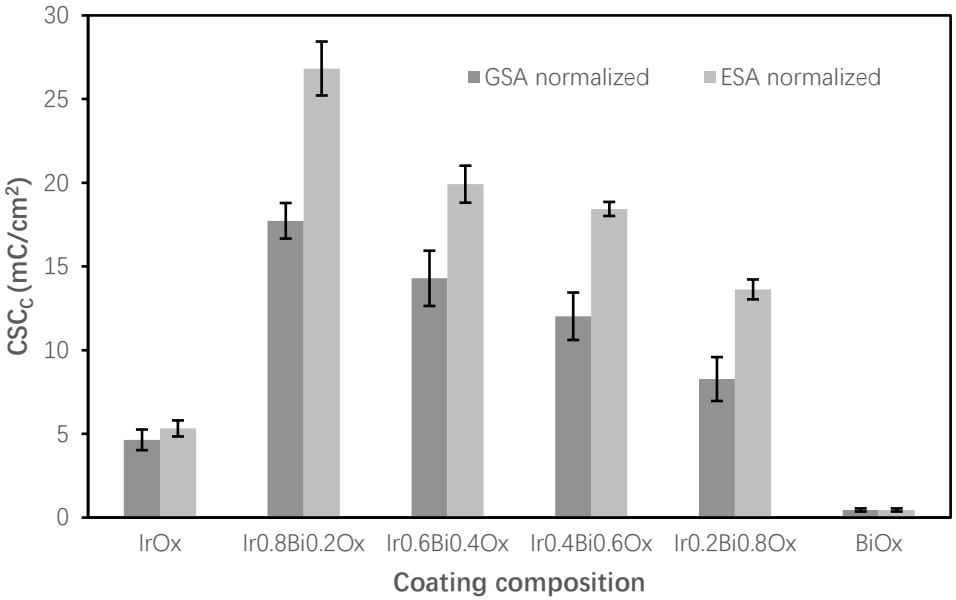


Figure 11. $CSC_c$ of $Ir_xBi_{1-x}$-oxide coating normalized with GSA and ESA. Measured at a scan rate of 50 mV/s in 0.1M PBS solution.

### *5.4.3 Impendence*

The impendence is another critical parameter for neural stimulating/recording electrode, reflecting the charge transfer resistance of the electrodes. The impendence of different coating compositions studied here, except for pure Bi-oxide, were measured at 0 V(SCE) using electrochemical impedance spectroscopy (EIS). The impedance at 1 kHz was then calculated as it corresponds to the millisecond's duration of an action potential and stimulating pulse[93], and the corresponding values are shown in Figure 12. It was found that $Ir_{0.8}Bi_{0.2}$-oxide exhibited significantly lower impedance than the other compositions, further confirming the superior behavior of this electrode composition.

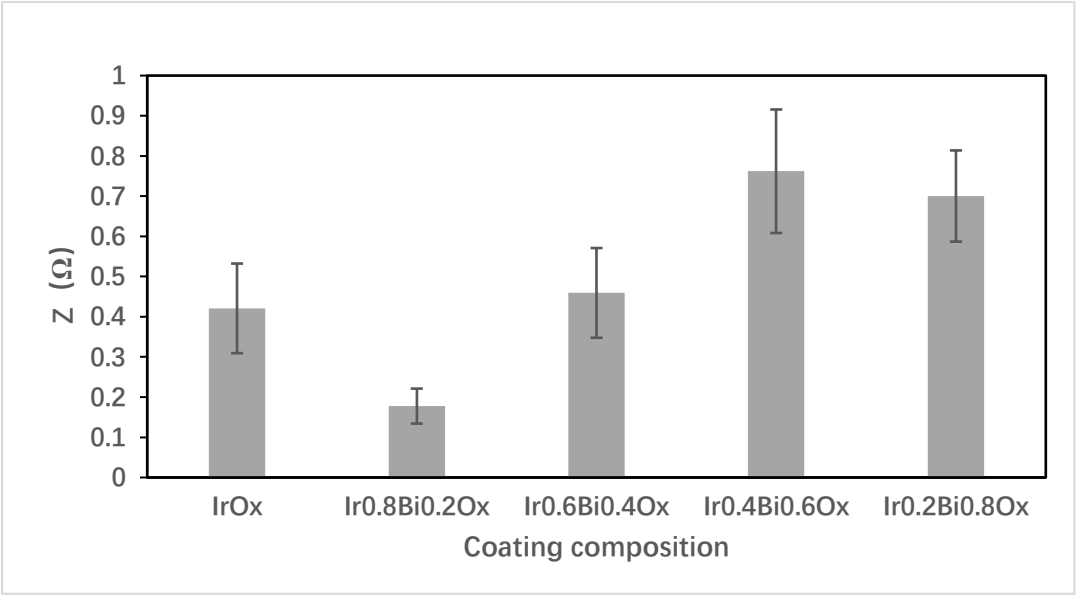


Figure 12. Impedance of $Ir_xBi_{1-x}$-oxide coating at 1 kHz at 0V bias (SCE), measured in 0.1 M PBS solution.

### *5.4.4 Stability*

The electrochemical stability of Ir-oxide (control) and $Ir_{0.8}Bi_{0.2}$-oxide was evaluated by long-term CV tests. The $CSC_c$ at the $20^{th}$ CV cycle and the $2000^{th}$ CV cycle and the impedance at 1 kHz before and after 2000 CV cycles are compared and the values are presented in Table 6. Degradation or loss of $CSC_c$, which is commonly reported in literature[94], was not observed in our work. By contract, all electrodes showed an increase in $CSC_c$ and a decrease in impedance after running 2000 CV cycles. This would be explained by surface and sub-surface morphology/structure changes during the electrochemical test[71]. The $Ir_{0.8}Bi_{0.2}$-oxide exhibited a slightly larger $CSC_c$ enhancement after long-term CV test but also a larger impedance decrease comparing with Ir-oxide electrodes. It was also noticed that after the stability test, the electrodes showed better hydrophilicity, which might also be the origin of the performance increase, while the quantitative evaluation of contact angle was not done yet.

The Ir ions and Bi ions concentration in electrolyte after long-term CV test was found to be below the detection limit of the ICP measurement, showing a good stability of thermally-deposited oxide coating.

Table 6. Comparison of $CSC_C$ and Impedance of Ir-oxide and $Ir_{0.8}Bi_{0.2}$-oxide before and after 2000 CV cycles.

| | | $CSC_C$ (mC/cm$^2$) | | | Impedance(Ω) | | |
|---|---|---|---|---|---|---|---|
| | Sample number | 20th CV cycle | 2000 CV cycle | Increase | New | After 2000 CV cycle | Decrease |
| Ir-Oxide | 1 | 5.55 | 6.0 | 8.8% | 0.31 | 0.28 | 10.0% |
| | 2 | 6.80 | 7.67 | 12.9% | 0.27 | 0.20 | 24.8% |
| | 3 | 5.11 | 5.67 | 10.9% | 0.31 | 0.31 | 8.7% |
| | Ave | 5.82 | 6.46 | 11.0% | 0.30 | 0.26 | 11.3% |
| $Ir_{0.8}Bi_{0.2}$-oxide | 1 | 18.09 | 23.24 | 28.5% | 0.12 | 0.12 | 4.0% |
| | 2 | 16.65 | 19.42 | 16.6% | 0.23 | 0.20 | 15.6% |
| | 3 | 14.02 | 15.92 | 13.5% | 0.20 | 0.17 | 13.9% |
| | Ave | 16.25 | 19.53 | 19.5% | 0.19 | 0.16 | 12.45% |

## 5.5 Cell culture biocompatibility: cell viability and neuron morphologies.

To test the biocompatibility of thermally-prepared Ir-oxide and $Ir_{0.8}Bi_{0.2}$-oxide electrodes, disassociated spinal cord cell embryonic day 13 mouse embryos were dropped on the electrode surface. After 40 DIV *in vitro* cultivation, differentiated cells can be distinguished[82]. Figure 13 (a-c) shows the micrographs taken from the surface of a coverslip, Ir-oxide, and $Ir_{0.8}Bi_{0.2}$-oxide with neurofilament marked in green, tubulin marked in red, and nuclear marked in blue. It is noticed that neurons exhibited a nonuniform density and differential stage distribution among the surfaces, and similar pattern present on Ir-oxide was also found on $Ir_{0.8}Bi_{0.2}$-oxide. As in Figure 13b, red arrow, the neuron dendritic outreaching is restricted in certain pathway, which is possibly because of the geometric factors as the coating surface exhibited a hilly "crack-

mud" morphology under SEM, Figure 6[95].

Neurons was labelled in red by Tuj1 as it responds to tubulin presence in neurons only. A well differentiated motor neuron is found in the center of Figure 13c with clear tubulin expression found. Some small star-shaped cells found at the edge of the vision field (indicated by a red arrow) with no tubulin expression in the corresponding area (red rectangular in Figure 13d) would be predicted as microglial cells[96]. The rest cells with their nuclear labelled in blue might be other supporting cells for neurons which differentiate from embryonic spinal cord cells.

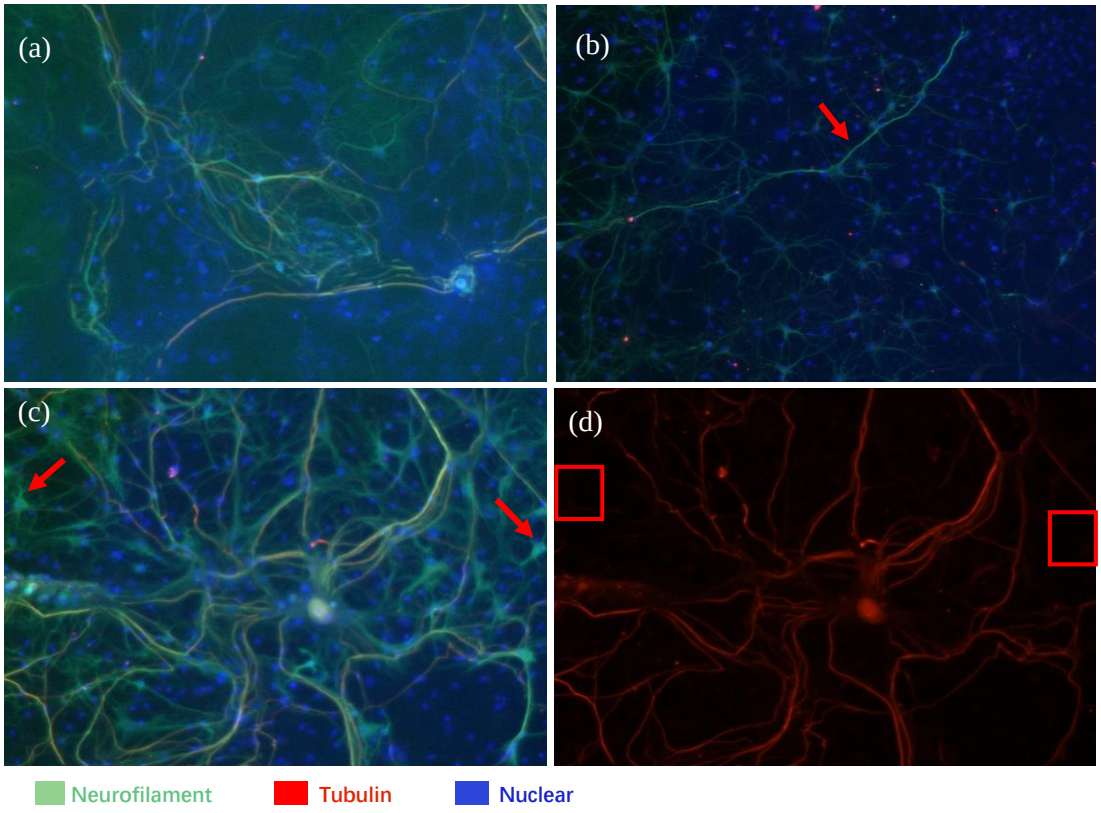


Figure 13. Micrographs of cells living on the substrate surface after 40 DIV with neurofilament, tubulin, and nuclear labelled in green, red, and blue, respectively. (a) on a coverslip; (b) on Ir-oxide; (c) on $Ir_{0.8}Bi_{0.2}$-oxide; (d) on $Ir_{0.8}Bi_{0.2}$-oxide with the only tubulin showing.

The total number of living cells on substrates is showing in Figure 14. A large deviation was noticed because of the heterogeneous distribution of cells. The average number of cells in the vision filed did not show significant difference. It should be note that the

coverslips were pre-treated with ploy-L-lysine and Matrigel, which would enhance the neuron attachment, while the metal oxide substrates were not treated, so the similar number of cells staying on the surface of coverslips and electrodes indicated that the metal oxides surface is neuron attachment friendly. However, the numerical comparison of total cells surviving on the substrate surface is not enough to prove the metal oxide coating has biocompatibility as good as treated coverslips because the initial loading of cells on each substrate from cells dropping was hard to control as the cells culture may flow around.

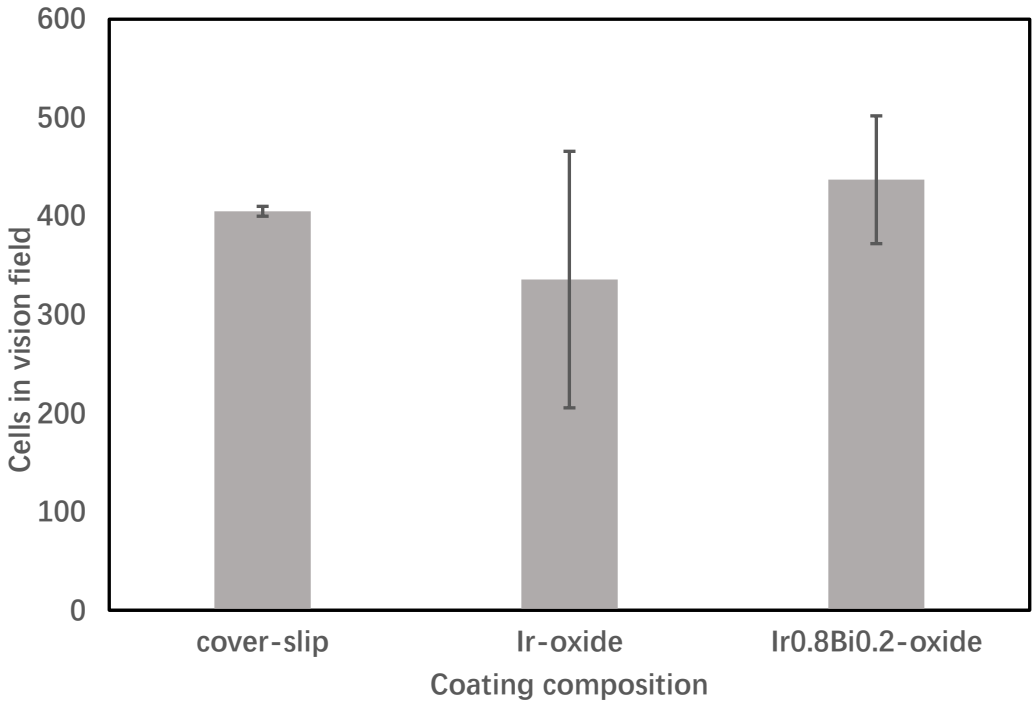


Figure 14. Cells survival after 40 DIV culturing on the top of substrates.

# 6. Conclusions:

$Ir_xBi_{1-x}$-oxide (x=0, 0.2, 0.4, 0.6, 0.8, 1) electrodes were fabricated from thermal deposition of precursor solution of Ir (III) and Bi (III) salts on a Ti substrate. The coating layers were found consisting of multi-oxidation states of Ir and/or Bi.

The charge storage capacitance and impedance were found to vary with Ir/Bi ratio. $Ir_{0.8}Bi_{0.2}$-oxide exhibiting the highest $CSC_c$ 17.73 $mC/cm^2$ (geometric surface area), which is almost five times larger than pure Ir-oxide. A further increase the proportion of Bi resulted in a decrease of $CSC_c$. After normalizing $CSC_c$ with respect to the electrochemically active surface area, in order to evaluate the intrinsic behavior of the coatings, the $Ir_{0.8}Bi_{0.2}$-oxide still exhibited the highest $CSC_c$, 26.8 $mC/cm^2$, which is five-fold of that of the state-or-the-art Ir-oxide. This good performance of $Ir_{0.8}Bi_{0.2}$-oxide was explained on the basis of improved surface and sub-surface morphology/structure that facilities protons transfer so that redox species in deeper layers under the surface get involved in faradaic reaction, providing extra charge injection. $Ir_{0.8}Bi_{0.2}$-oxide also exhibited the lowest impedance which could also be explained on the basis of increased capacitance and low proton transfer resistance. $Ir_{0.8}Bi_{0.2}$-oxide and Ir-oxide exhibited similar and good stability under long-term CV test. No obvious difference in cytotoxicity of the oxides was observed. The research presented here evidences that $Ir_{0.8}Bi_{0.2}$-oxide represents a good candidate as the coating material of neuron electrodes, with properties superior to those of the current state-of-the-art Ir-oxide.

# 7. Future work

This work preliminarily characterized and evaluated the electrochemical properties of $Ir_xBi_{1-x}$-oxide (x=0, 0.2, 0.4, 0.6, 0.8, 1) fabricated by thermal deposition. Although $Ir_{0.8}Bi_{0.2}$-oxide shows better performance than Ir-oxide control, further research needs to be done before confirming $Ir_{0.8}Bi_{0.2}$-oxide is indeed a better material than the state-of-arts Ir-oxide as the neural stimulating electrode.

The $Ir_{0.8}Bi_{0.2}$-oxide showed the best results among $Ir_xBi_{1-x}$-oxides (x=0, 0.2, 0.4, 0.6, 0.8, 1), but a composition with better performance might exist between Ir-oxide and $Ir_{0.8}Bi_{0.2}$-oxide or between $Ir_{0.8}Bi_{0.6}$-oxide and $Ir_{0.6}Bi_{0.4}$-oxide. Future work will be done with narrow composition interval as 5% to specify the best composition.

The better electrochemical performance of $Ir_{0.8}Bi_{0.2}$-oxide is attributed to lattice structural change that facilitates ion transfer. This could be further confirmed by CV scanning under different scan rate and comparing the charge storage capacity.

Increased hydrophilicity and $CSC_c$ were observed after long-term CV testing, and the origin of these difference are attributed to morphology/structure change, but TEM, SEM, AFM characterization and contact angle tests after long-term CV need to be done.

The charge storage capacity is just an indicator of charge injection capacity, and the electrode size in this work is by far larger than the real size of neural stimulating electrodes. Thus, the true charge injection capacity of $Ir_{0.8}Bi_{0.2}$-oxide with real electrode size under real stimulation protocol need to be evaluated.

The cytotoxicity evaluation of this work is more qualitative than quantitative, and it was done *in vitro* under a passive condition without stimulating pulses applied. The

biocompatibility of the $Ir_{0.8}Bi_{0.2}$-oxide needs to be evaluated *in vivo* before applying $Ir_xBi_{1-x}$-oxide in neural prosthetics.

# Appendix A. Electrochemical Active Surface Area

To measure the electrochemical active surface area (ESA), CV tests were performed at different scan rates in a solution of 2 mM potassium ferricyanide in 0.1 M potassium nitrate, Figure 14.

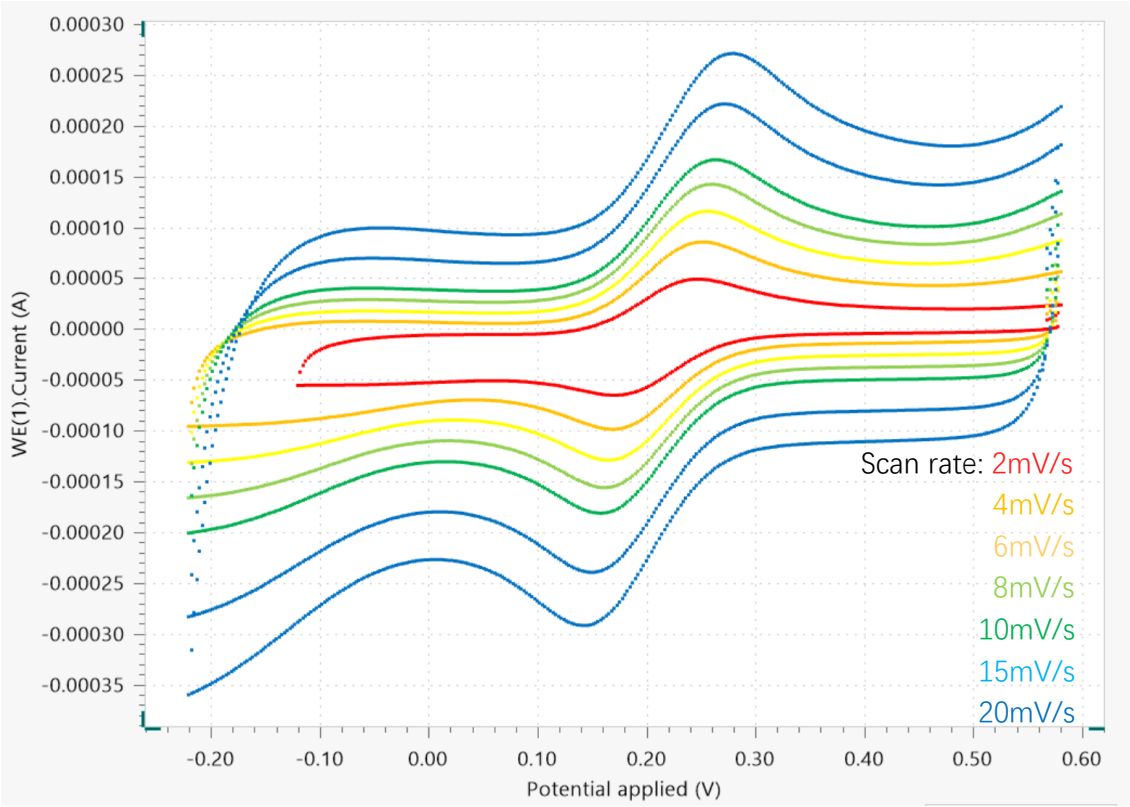


Figure 14. CV plots under different scan rates from 2 mV/s to 20 mV/s

The current peak located at ~0.15 V and ~0.25 V refers to the reduction and oxidation between Fe(II) and Fe(III). Cathodal peak current was abstracted by removing background current. Figure 15 shows an example of the linear relation between peak current and the square root of scan rates. The electrochemical surface area would then be calculated from the slope.

From Randle-Sevcik Equation (Equation 7 in Experimental section):

$$slope = kn^{3/2}AD^{0.5}C_b$$

$$A = slope/(kn^{\frac{3}{2}}D^{0.5}C_b)$$

where k = 268; n is the number of electrons transferred per molecule of ferricyanide, which is 1; A is the area of the electrode in $cm^2$; D is the diffusion coefficient in $cm^2/s$, which is taking as $6.2\times10^{-6}$ for 2mM $K_3Fe(CN)_6$; $C_b$ is the solution concentration in mol/L, which is 0.002.

$$A = \frac{9.1 \times 10^{-4}}{268 \times 1 \times (6.2 \times 10^{-6})^{0.5} \times 0.002}$$

$$=0.68\ cm^2$$

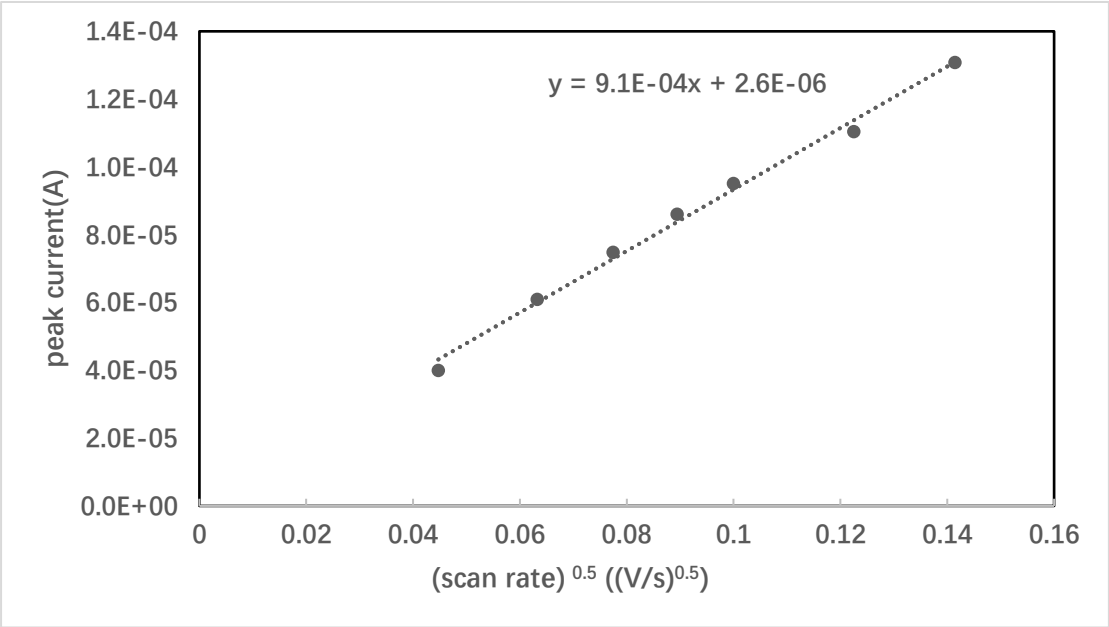


Figure 15. Linear fitting of the square root of scan rate and cathodic peak current.

The calculated ESA of all composition except pure Bi-oxide, which was not responding to ferro/ferri redox, are showing in Figure 16.

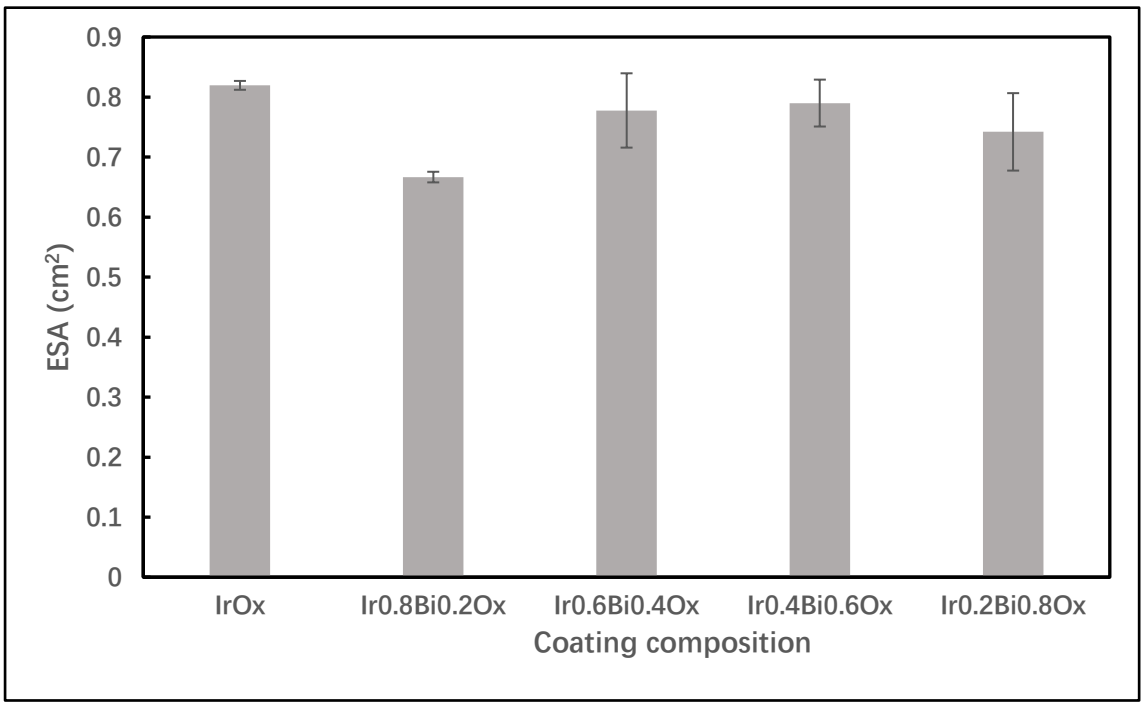


Figure 16. Electrochemically active surface area (ESA) of each composition except Bi-oxide which did not respond to redox of ferro.

# Reference


1. Elcap. *Double-layer capacitance*. Available from: https://commons.wikimedia.org/wiki/User:Elcap.
2. Cogan, S.F., *Neural stimulation and recording electrodes.* Annu Rev Biomed Eng, 2008. **10**: p. 275-309.
3. Shire, D.B., et al., *Development and implantation of a minimally invasive wireless subretinal neurostimulator.* IEEE Trans Biomed Eng, 2009. **56**(10): p. 2502-11.
4. Schmidt, E.M., et al., *Feasibility of a visual prosthesis for the blind based on intracorticai microstimulation of the visual cortex.* Brain, 1996. **119**: p. 507-522.
5. Tykocinski, M., et al., *Chronic electrical stimulation of the auditory nerve using high surface area (HiQ) platinum electrodes.* Hearing Research, 2001. **159**(1-2): p. 53-68.
6. Hochberg, L.R., et al., *Neuronal ensemble control of prosthetic devices by a human with tetraplegia.* Nature, 2006. **442**(7099): p. 164-71.
7. Benabid, A.L., et al., *Deep brain stimulation of the subthalamic nucleus for the treatment of Parkinson's disease.* Lancet Neurol, 2009. **8**(1): p. 67-81.
8. Schalk, G., et al., *Brain-computer interfaces (BCIs): detection instead of classification.* J Neurosci Methods, 2008. **167**(1): p. 51-62.
9. Kotov, N.A., et al., *Nanomaterials for Neural Interfaces.* Advanced Materials, 2009. **21**(40): p. 3970-4004.
10. Rui, Y.F., et al., *Parylene-based implantable platinum-black coated wire microelectrode for orbicularis oculi muscle electrical stimulation.* Biomed Microdevices, 2012. **14**(2): p. 367-73.
11. Hai, A., et al., *Changing gears from chemical adhesion of cells to flat substrata toward engulfment of micro-protrusions by active mechanisms.* J Neural Eng, 2009. **6**(6): p. 066009.
12. Weiland, J.D., et al., *In vitro electrical properties for iridium oxide versus titanium nitride stimulating electrodes.* IEEE Trans Biomed Eng, 2002. **49**(12 Pt 2): p. 1574-9.
13. Rose TL., et al., *Assessment of capacitor electrodes for intracortical neura stimulation.* . J. Neurosci. Methods, 1985. **12**.
14. Schmidt, E.M., et al., *Intracortical capacitor electrodes: preliminary evaluation.* J Neurosci Methods, 1982. **5**(1-2): p. 33-9.
15. Cui, X.Y. and D.C. Martin, *Electrochemical deposition and characterization of poly(3,4-ethylenedioxythiophene) on neural microelectrode arrays.* Sensors and Actuators B-Chemical, 2003. **89**(1-2): p. 92-102.
16. Abidian, M.R. and D.C. Martin, *Experimental and theoretical characterization of implantable neural microelectrodes modified with conducting polymer nanotubes.* Biomaterials, 2008. **29**(9): p. 1273-83.
17. Park, D.W., et al., *Fabrication and utility of a transparent graphene neural electrode array for electrophysiology, in vivo imaging, and optogenetics.* Nat Protoc, 2016. **11**(11): p. 2201-2222.
18. Lu, Y., et al., *Flexible Neural Electrode Array Based-on Porous Graphene for Cortical*

*Microstimulation and Sensing.* Sci Rep, 2016. **6**: p. 33526.
19. Ansaldo, A., et al., *Superior Electrochemical Performance of Carbon Nanotubes Directly Grown on Sharp Microelectrodes.* Acs Nano, 2011. **5**(3): p. 2206-2214.
20. Wang K., et al., *Neural Stimulation with a Carbon Nanotube Micreoelectrode Array.* NANO LETTERS, 2006. **6**: p. 2043-2048.
21. Keefer, E.W., et al., *Carbon nanotube coating improves neuronal recordings.* Nat Nanotechnol, 2008. **3**(7): p. 434-9.
22. Kelliher, E.M. and T.L. Rose, *Evaluation of Charge Injection Properties of Thin Film Redox Materials for use as Neural Stimulation Electrodes.* MRS Proceedings, 2011. **110**.
23. Kim, S., et al., *Integrated wireless neural interface based on the Utah electrode array.* Biomed Microdevices, 2009. **11**(2): p. 453-66.
24. Cogan, S.F., et al., *Sputtered iridium oxide films (SIROFs) for low-impedance neural stimulation and recording electrodes.* Conf Proc IEEE Eng Med Biol Soc, 2004. **6**: p. 4153-6.
25. Troyk P.R., et al., *"Safe" charge-injection waveforms for iridium oxide (AIROF) microelectrodes* 26th Annual Intemational Conference ofthe IEEE EMBS, 2004.
26. Cogan, S.F., et al., *Over-pulsing degrades activated iridium oxide films used for intracortical neural stimulation.* J Neurosci Methods, 2004. **137**(2): p. 141-50.
27. Ross D., et al., *Electrodeposited IrOx for Neural Stimulation and Recording Electrodes.* IEEE Transactions on Neural Systems and Rehabilitation Engineering, 2001. **9**.
28. Zeng, Q., et al., *Electrodeposited Iridium Oxide on Platinum Nanocones for Improving Neural Stimulation Microelectrodes.* Electrochimica Acta, 2017. **237**: p. 152-159.
29. Carretero, N.M., et al., *IrOx-carbon nanotube hybrids: a nanostructured material for electrodes with increased charge capacity in neural systems.* Acta Biomater, 2014. **10**(10): p. 4548-58.
30. Carretero, N.M., et al., *Enhanced Charge Capacity in Iridium Oxide-Graphene Oxide Hybrids.* Electrochimica Acta, 2015. **157**: p. 369-377.
31. Moral-Vico, J., et al., *Nanocomposites of iridium oxide and conducting polymers as electroactive phases in biological media.* Acta Biomaterialia, 2014. **10**(5): p. 2177-2186.
32. Deng, W.T., et al., *Electrochemical capacitors utilising transition metal oxides: an update of recent developments.* Rsc Advances, 2011. **1**(7): p. 1171-1178.
33. Sarma, B., et al., *Redox-Induced Enhancement in Interfacial Capacitance of the Titania Nanotube/Bismuth Oxide Composite Electrode.* Acs Applied Materials & Interfaces, 2013. **5**(5): p. 1688-1697.
34. Hwang, Y.C., et al., *Chemical composition, radiopacity, and biocompatibility of Portland cement with bismuth oxide.* Oral Surg Oral Med Oral Pathol Oral Radiol Endod, 2009. **107**(3): p. e96-102.
35. Sardar, K., et al., *Bismuth Iridium Oxide Oxygen Evolution Catalyst from Hydrothermal Synthesis.* Chemistry of Materials, 2012. **24**(21): p. 4192-4200.
36. BouchARD, R.J., *Oxibes of Cubic Crystal Structure Containing Bismuth and at Least One of Ruthenium And Iridium*. 1971: US.

37. *McNeal, D.R., 2000 years of electrical stimulation, in Functional Electrical Stimulation, F.T. Hambrecht and J.B. Reswick, Eds. New York: Marcel Dekker, 1977, p. 3–33.*
38. Woeppel, K., et al., *Recent Advances in Neural Electrode-Tissue Interfaces.* Curr Opin Biomed Eng, 2017. **4**: p. 21-31.
39. Zeng, F.G., et al., *Cochlear implants: system design, integration, and evaluation.* IEEE Rev Biomed Eng, 2008. **1**: p. 115-42.
40. Daniel J., et al., *Neuroengineering*. 2008: Taylor & Francis Group
41. Stieglitz, T., *Development of a micromachined epiretinal vision prosthesis.* J Neural Eng, 2009. **6**(6): p. 065005.
42. Graupe, D., et al., *A critical review of EMG-controlled electrical stimulation in paraplegics.* Crit Rev Biomed Eng, 1987. **15**(3): p. 187-210.
43. Keith M1., et al., *Implantable functional neuromuscular stimulation in the tetraplegic hand.* J Hand Surg Am, 1989. **14**(3): p. 524-530.
44. Hochberg, L.R., et al., *Reach and grasp by people with tetraplegia using a neurally controlled robotic arm.* Nature, 2012. **485**(7398): p. 372-U121.
45. Stieglitz, T., et al., *Implantable biomedical microsystems for neural prostheses.* Ieee Engineering in Medicine and Biology Magazine, 2005. **24**(5): p. 58-65.
46. Brice, J. and L. McLellan, *Suppression of intention tremor by contingent deep-brain stimulation.* Lancet, 1980. **1**(8180): p. 1221-2.
47. *NEUROPACE RNS system*.
48. Luan, S., et al., *Neuromodulation: present and emerging methods.* Front Neuroeng, 2014. **7**: p. 27.
49. Brummer, S.B. and M.J. Turner, *Electrochemical considerations for safe electrical stimulation of the nervous system with platinum electrodes.* IEEE Trans Biomed Eng, 1977. **24**(1): p. 59-63.
50. Lapicque, L., *Quantitative Investigation of Electrial Nerve Excitation Treated As Polarization.* J Physiol (Paris), 1907. **9**.
51. Warman, E.N., et al., *Modeling the Effects of Electric-Fields on Nerve-Fibers - Determination of Excitation Thresholds.* Ieee Transactions on Biomedical Engineering, 1992. **39**(12): p. 1244-1254.
52. Marin, C. and E. Fernandez, *Biocompatibility of intracortical microelectrodes: current status and future prospects.* Front Neuroeng, 2010. **3**: p. 8.
53. Kuncel, A.M. and W.M. Grill, *Selection of stimulus parameters for deep brain stimulation.* Clin Neurophysiol, 2004. **115**(11): p. 2431-41.
54. Rizzo, J.F., et al., *Perceptual efficacy of electrical stimulation of human retina with a microelectrode array during short-term surgical trials.* Invest Ophthalmol Vis Sci, 2003. **44**(12): p. 5362-9.
55. Merrill, D.R., et al., *Electrical stimulation of excitable tissue: design of efficacious and safe protocols.* J Neurosci Methods, 2005. **141**(2): p. 171-98.
56. Rose, L.S., et al., *The Electrochemistry of Electrical Stimulation.* Annual International Conference of the IEEE Engineering in Medicine and Biology Society, 1990. **12**.
57. Robblee, T.L., et al.,*Electrical stimulation with Pt electrodes. VII. Electrochemically*

*safe charge.* IEEE Trans Biomed Eng, 1990. **37**.
58. Beebe, X. and T.L. Rose, *Charge Injection Limits of Activated Iridium Oxide Electrodes with 0.2ms Pulses in Bicarbonate Buffered Saline.* Ieee Transactions on Biomedical Engineering, 1988. **35**(6): p. 494-495.
59. Cogan, S.F., et al., *Charge-injection waveforms for iridium oxide (AIROF) microelectrodes.* Proceedings of the 25th Annual International Conference of the Ieee Engineering in Medicine and Biology Society, Vols 1-4, 2003. **25**: p. 1960-1963.
60. Grill, W.M., et al., *Implanted neural interfaces: biochallenges and engineered solutions.* Annu Rev Biomed Eng, 2009. **11**: p. 1-24.
61. Rios, G., et al., *Nanofabricated Neural Probes for Dense 3-D Recordings of Brain Activity.* Nano Lett, 2016. **16**(11): p. 6857-6862.
62. Wise, K.D., et al., *Microelectrodes, microelectronics, and implantable neural microsystems.* Proceedings of the Ieee, 2008. **96**(7): p. 1184-1202.
63. Ghane-Motlagh, B., et al., *A Review of Microelectrode Array Technologies: Design and Implementation Challenges.* 2013 2nd International Conference on Advances in Biomedical Engineering (Abme 2013), 2013. **04**(08): p. 38-41.
64. Leber, M., et al., *Different methods to alter surface morphology of high aspect ratio structures.* Appl Surf Sci, 2016. **365**: p. 180-190.
65. Leber, M., et al., *Long term performance of porous platinum coated neural electrodes.* Biomed Microdevices, 2017. **19**(3): p. 62.
66. Wu, Y.J., et al., *Conformal deposition of Pt on titania nanotubes to produce a bio-electrode for neuro-stimulating applications.* Electrochemistry Communications, 2018. **88**: p. 61-66.
67. Negi, S., et al., *Neural electrode degradation from continuous electrical stimulation: comparison of sputtered and activated iridium oxide.* J Neurosci Methods, 2010. **186**(1): p. 8-17.
68. Lois S., et al., *The Electrochemistry of Electrical Stimulation.* Annual Intemational Conference of the IEEE Engineering in Medicine and Biology Society, 1990. **12**.
69. Wessling, B., et al., *RF-sputtering of iridium oxide to be used as stimulation material in functional medical implants.* Journal of Micromechanics and Microengineering, 2006. **16**(6): p. S142-S148.
70. Trasatti S., et al., *Eletrochemical Supercapacitors as Versatile Engergy Stores.* Platinum Metals Review, 1994. **38**: p. 46-56.
71. Ullah, N. and S. Omanovic, *Large charge-storage-capacity iridium/ruthenium oxide coatings as promising material for neural stimulating electrodes.* Materials Chemistry and Physics, 2015. **159**: p. 119-127.
72. Stilling, J., et al., *Ir-Ni oxide as a promising material for nerve and brain stimulating electrodes.* Journal of Electrochemical Science and Engineering, 2014. **4**(3).
73. Cruz, A.M., et al., *Graded conducting titanium–iridium oxide coatings for bioelectrodes in neural systems.* Thin Solid Films, 2013. **534**: p. 316-324.
74. Habibzadeh, S., et al., *Biocompatibility of Ir/Ti-oxide coatings: Interaction with platelets, endothelial and smooth muscle cells.* Applied Surface Science, 2014. **301**: p. 530-538.

75. Zhou, D.D., et al., *Conducting Polymers in Neural Stimulation Applications*, in *Implantable Neural Prostheses 2*. 2009. p. 217-252.
76. Cui, X.T., et al., *Poly (3,4-ethylenedioxythiophene) for chronic neural stimulation.* IEEE Trans Neural Syst Rehabil Eng, 2007. **15**(4): p. 502-8.
77. Voge, C.M. and J.P. Stegemann, *Carbon nanotubes in neural interfacing applications.* J Neural Eng, 2011. **8**(1): p. 011001.
78. Luo, X., et al., *Highly stable carbon nanotube doped poly(3,4-ethylenedioxythiophene) for chronic neural stimulation.* Biomaterials, 2011. **32**(24): p. 5551-7.
79. Du, Z.J., et al., *Electrically Controlled Neurochemical Release from Dual-Layer Conducting Polymer Films for Precise Modulation of Neural Network Activity in Rat Barrel Cortex.* Adv Funct Mater, 2018. **28**(12).
80. Lu, Y., et al., *Electrodeposited polypyrrole/carbon nanotubes composite films electrodes for neural interfaces.* Biomaterials, 2010. **31**(19): p. 5169-81.
81. Green, R.A., et al., *Novel neural interface for implant electrodes: improving electroactivity of polypyrrole through MWNT incorporation.* J Mater Sci Mater Med, 2008. **19**(4): p. 1625-9.
82. Roy, J., et al., *Glutamate potentiates the toxicity of mutant Cu/Zn-superoxide dismutase in motor neurons by postsynaptic calcium-dependent mechanisms.* Journal of Neuroscience, 1998. **18**(23): p. 9673-9684.
83. Vidales, A.G., et al., *The influence of addition of iridium-oxide to nickel-molybdenum-oxide cathodes on the electrocatalytic activity towards hydrogen evolution in acidic medium and on the cathode deactivation resistance.* Electrochimica Acta, 2019. **302**: p. 198-206.
84. Duan, F., et al., *Synthesis and photocatalytic behaviour of 3D flowerlike bismuth oxide formate architectures.* Materials Letters, 2010. **64**(14): p. 1566-1569.
85. Augustynski, J., et al., *Esca Study of the State of Iridium and Oxygen in Electrochemically and Thermally Formed Iridium Oxide-Films.* Journal of Electroanalytical Chemistry, 1984. **160**(1-2): p. 233-248.
86. Pfeifer, V., et al., *The electronic structure of iridium and its oxides.* Surface and Interface Analysis, 2016. **48**(5): p. 261-273.
87. Peuckert, M., *Xps Study on Thermally and Electrochemically Prepared Oxidic Adlayers on Iridium.* Surface Science, 1984. **144**(2-3): p. 451-464.
88. Vineet S., et al., *Characterisation of Thin Films of Bismuth Oxide by X-Ray Photoelectron Spectroscopy.* Journal of Electron Spectroscopy and Related Phenomena, 1982. **25**.
89. Luo, Y.R., *Comprehensive Handbook of Chemical Bond Energies*. 2007 CRC Press.
90. Habibzadeh, S., et al., *Surface and Electrochemical Characterization of IrTi-Oxide Coatings: Towards the Improvement of Radiopacity for Coronary Stent Applications.* International Journal of Electrochemical Science, 2013. **8**(5): p. 6291-6310.
91. Mailley S.C., et al., *Electrochemical and structural characterizations of electrodeposited iridium oxide thin film electrodes applied to neruostimulating electrical signal.* Materials Science and Engineering, 2002. **21**.
92. Ching, S., et al., *Cyclic Voltammetry with Ultramicroelectrodes.* Journal of Chemical

Education, 1994. **71**(7): p. 602-605.
93. Parker, R.A., et al., *The use of a novel carbon nanotube coated microelectrode array for chronic intracortical recording and microstimulation.* 2012 Annual International Conference of the Ieee Engineering in Medicine and Biology Society (Embc), 2012: p. 791-794.
94. Peixoto, N., et al., *Charge Storage: Stability Measures in Implantable Electrodes.* 2009 Annual International Conference of the Ieee Engineering in Medicine and Biology Society, Vols 1-20, 2009: p. 658-661.
95. Merz, M. and P. Fromherz, *Silicon chip interfaced with a geometrically defined net of snail neurons.* Advanced Functional Materials, 2005. **15**(5): p. 739-744.
96. Polikov, V.S., et al., *Response of brain tissue to chronically implanted neural electrodes.* J Neurosci Methods, 2005. **148**(1): p. 1-18.